CHAPTER IV
RESULTS AND DISCUSSIONS

The characterization of the glass sample involved an in-depth analysis of its crystal structure, which was meticulously investigated through X-ray diffraction techniques (XRD). This method provided valuable insights into the internal arrangement and properties of the glass material, contributing to a comprehensive understanding of its structural composition. In addition, we have conducted extensive studies in various aspects. The electrochemical properties were assessed through charge-discharge curve analysis. Furthermore, impedance values within the battery electrodes were precisely measured using the Electrochemical Impedance Spectroscopy (EIS) technique. Additionally, the energy density measurements of glass electrodes were carried out using cyclic voltammetry (CV). X-ray Absorption Near Edge Structure (XANES) provided information on the electronic and structural properties, and Extended X-ray Absorption Fine Structure (EXAFS) revealed the local structural environment around specific atoms.

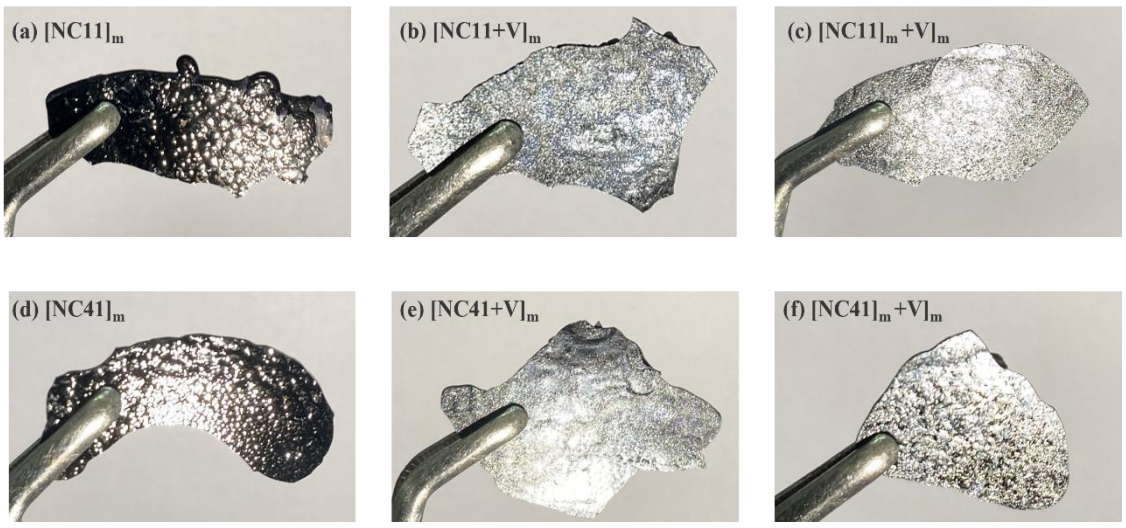

Figure 4.1 Show the physical and morphological properties of samples a) $[NC11]_m$, b) $[NC11+V]_m$, c) $[NC11]_m+V]_m$, d) $[NC41]_m$, e) $[NC41+V]_m$ and f) $[NC41]_m+V]_m$ respectively.

4.1 Physical characteristics

Figure 4.1 illustrates the physical surface of LBO glass samples that have been mixed with varying concentrations of Ni/Co_3O_4 and V_2O_5. The prepared glass samples, after the firing process, exhibit a dense and smooth surface structure. The addition of cobalt, in different concentrations, results in some samples displaying a black coloration, indicating successful incorporation of the dopants into the glass matrix. The glass produced appears to be of high quality, characterized by its density and a uniform surface.

One of the notable features of the glass is its hard yet brittle nature, a typical characteristic of glass materials. This brittleness makes the material prone to breaking, often resulting in sharp cracks when fractured. Despite this, the surface of the glass retains a shiny, reflective gleam, further confirming the integrity of the glass's surface and its smoothness. These qualities suggest that the material has maintained its glassy properties while incorporating the metallic oxides, which likely contribute to its coloration and potentially to other physical and chemical properties. The high quality and density of the glass surfaces are key indicators of successful preparation, which will influence the material's application in various fields, such as energy storage or electronic devices.

4.2 The crystal structure was investigated by X-ray diffraction

The phase formation of the glass samples was confirmed through X-ray diffraction (XRD) using a Bruker D8 Advance with a Cu k alpha source (λ = 1.54 Å), Detectoe 1 Dimesional conpound silicon strip, High temp 25-1600°C, 40kv 40mA. XRD data were collected at room temperature over a 2θ range of 10° to 80°, with a scanning speed of 2.4 deg/min and a step size of 0.02 s. From the experimental results of making glass samples according to the formula in this work, it was found that the phase verification results of XRD patterns It was found that it was an imperfect amorphous phase. as shown in Figure 4.2 and Table 4.2, calculated using Equation 4.1.

$$\text{Crystallinity (\%)} = \frac{\text{Area of crystalline peaks}}{\text{Area of all peaks (crystalline+amorphous)}} \times 100 \quad \text{Equation 4.1}$$

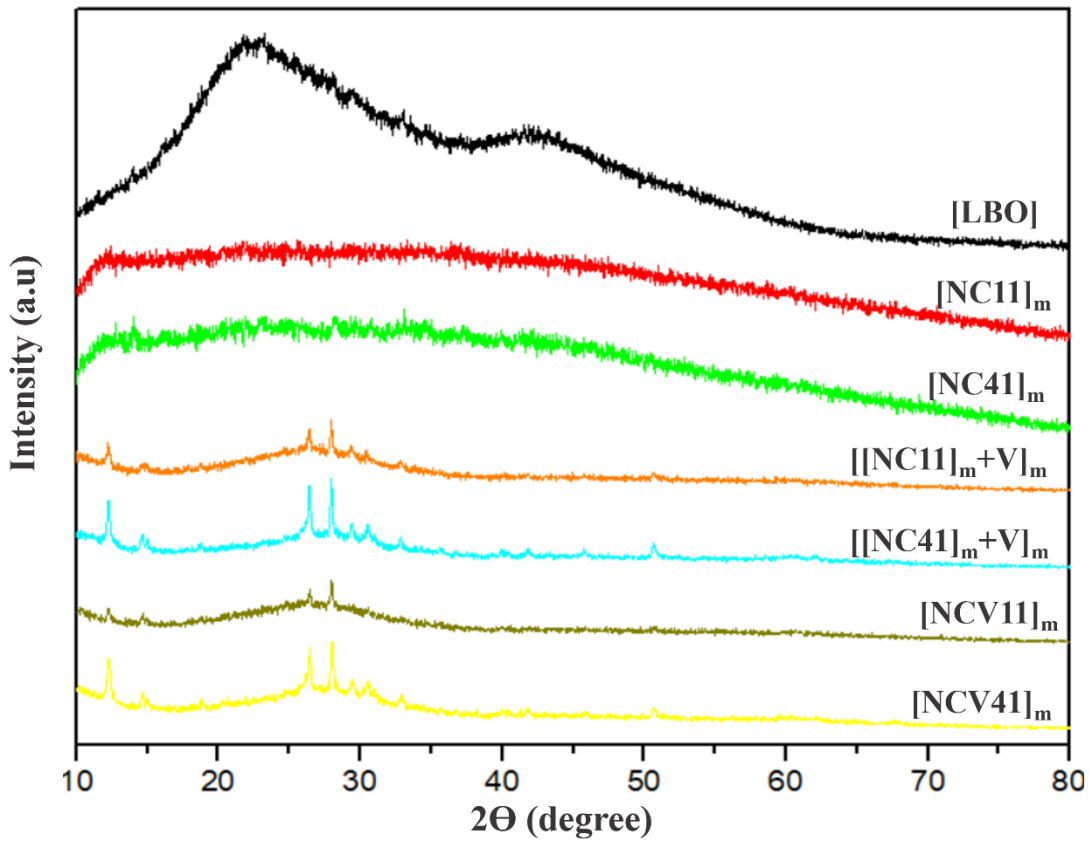

Figure 4.2 The XRD patterns of LBO, $[NC11]_m$, $[NC41]_m$, $[NC11]_m+V]_m$, $[NC41]_m+V]_m$, $[NC11+V]_m$ and $[NC41+V]_m$ respectively.

The $[NC11]_m$ and $[NC41]_m$ sample exhibits a glassy nature with less than 3% crystallinity. In comparison, the $[[NC11]_m+V]_m$, $[[NC41]_m+V]_m$, $[NC11+V]_m$ and $[NC41+V]_m$ samples show about 30% crystallinity, indicating that adding V_2O_5, followed by sintering, induces the formation of glass ceramics. To determine the crystalline structure, the observed peaks were analyzed using Jana2006 software and the Materials Project model, identifying them as corresponding to Lithium Hexaborate ($Li_6B_4O_9$). The peaks in the $[[NC11]_m+V]_m$, $[[NC41]_m+V]_m$, $[NC11+V]_m$ and $[NC41+V]_m$ samples matched the characteristic planes of $Li_6B_4O_9$, such as (021), (100), and (11-2), as shown in figure 4.3. The base glass, referred to as Lithium Tetraborate ($Li_2B_4O_7$ or LBO), exhibited an amorphous structure (black line, figure 4.2).

Table 4.1 Shows the percentage of crystallinity of the material of all sample.

No	Sum of area of crystalline peaks	Area of all peaks	Crystallinity of this material
$[NC11]_m$	65	4642	1 %
$[NC41]_m$	186	6900	3 %
$[NC11]_m+V]_m$	402	2426	17 %
$[NC41]_m+V]_m$	784	2611	30 %
$[NC11+V]_m$	280	2471	11 %
$[NC41+V]_m$	786	2682	29 %

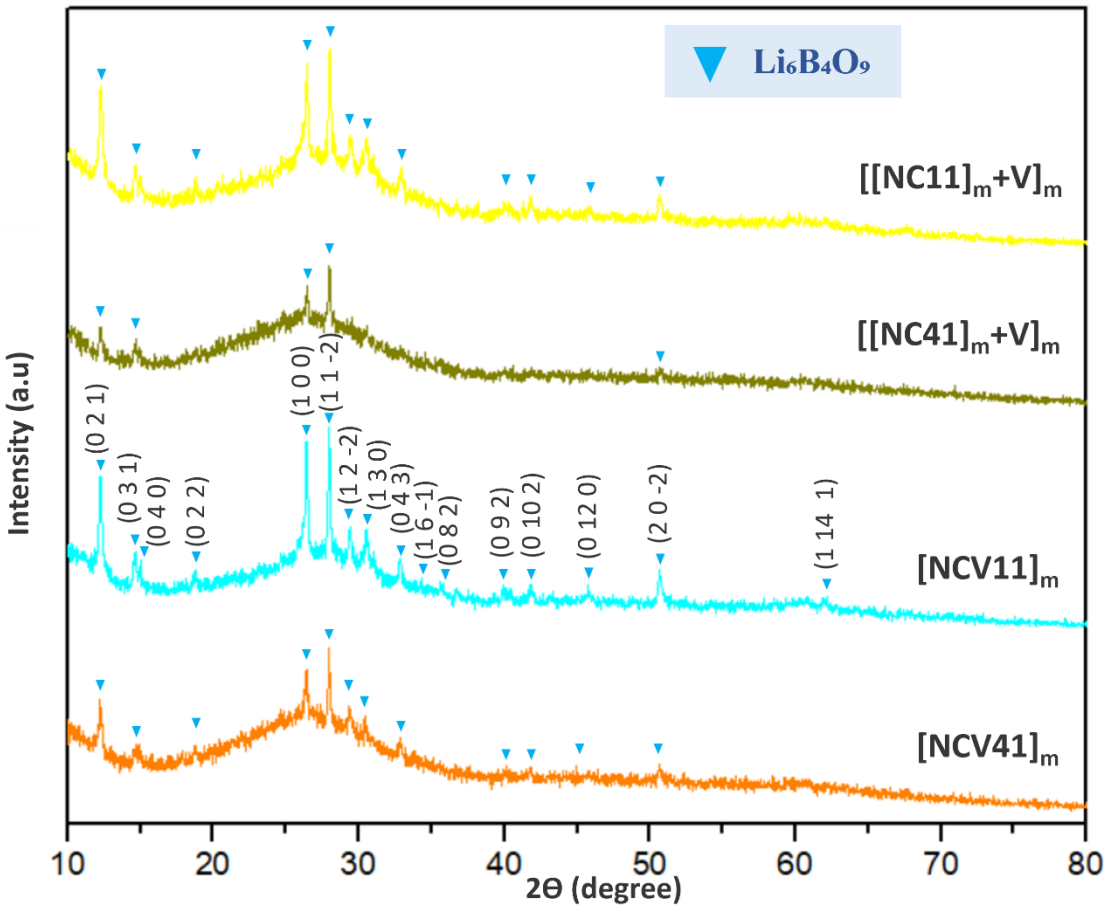

Figure 4.3 XRD patterns of the $Li_6B_4O_9$ ceramic.

When LBO was mixed with Ni/Co and subjected to a second sintering process ($[NC]_m$), it retained its amorphous nature (red and green line). The study of the $Li_6B_4O_9$

peak revealed that the $[[NC]_m + V]_m$ sample exhibited a higher peak intensity compared to the $[NCV]_m$ sample. This indicates that the sample with a lower peak intensity possesses a more amorphous nature (Figure 4.4). The improved crystallinity in the $[[NC]_m + V]_m$ sample is attributed to undergoing three melting cycles. These repeated cycles facilitated more thorough crystallization than samples that underwent only two cycles. Consequently, the crystalline structure in the $[[NC]_m + V]_m$ sample became more defined and complete after the additional melting process.

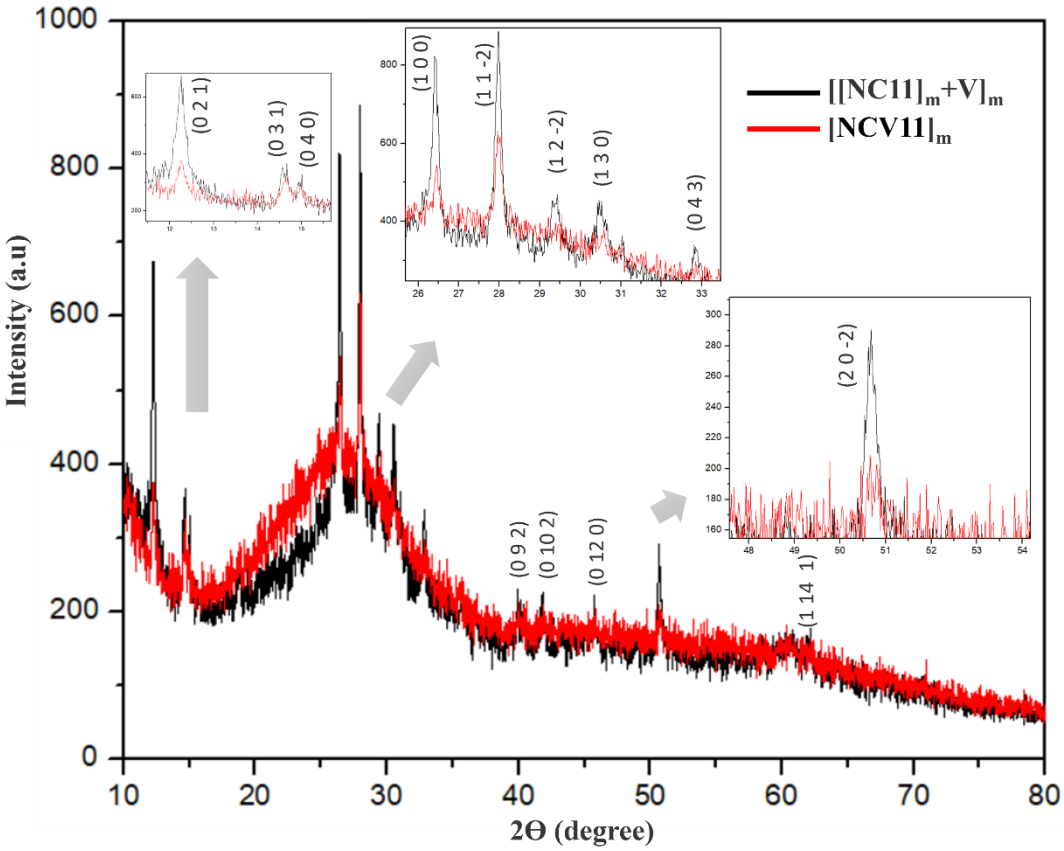

Figure 4.4 The graph compares the intensity of the $Li_6B_4O_9$ peak between the samples $[[NC]_m + V]_m$ and $[NCV]_m$.

$Li_6B_4O_9$ exhibits a monoclinic crystal structure with refined cell parameters of a = 3.39 Å, b = 23.65 Å, c = 9.73 Å, and angles α = 90.00°, β = 107.90°, and γ = 90.00°, resulting in a unit cell volume of 743.42 Å³. The crystal system is monoclinic, with a Hall number of -P 2ybc and an International Number of 14, classified under the space

group $P2_1/c$. It has a density of 2.04 $g{\cdot}cm^{-3}$ and possible oxidation states of Li^{+}, B^{3+}, and O^{2-}. There are four formula units per cell, with the lithium, boron, and oxygen atoms occupying the Wyckoff general position 4e, with full occupancy. The boron atoms form planar BO_3 units, linked at their vertices to create quasi-planar B_4O_9 groups, which stack perpendicular to the [100] direction. Lithium atoms are located between these B_4O_9 platelets, coordinated by oxygen atoms within distorted tetrahedra and trigonal bipyramids. The Li–O bond lengths range from 1.90 to 2.40 Å, contributing to varying lithium coordination across the structure. This complex arrangement contributes to the unique electrochemical properties of $Li_6B_4O_9$ (G. Rousse, B. Baptiste, and G. Lelong, 2014; G. l. Rousse, B. Baptiste, and G. r. Lelong, 2014; Zhou, Pang, Wang, Qi, and Reaney, 2018).

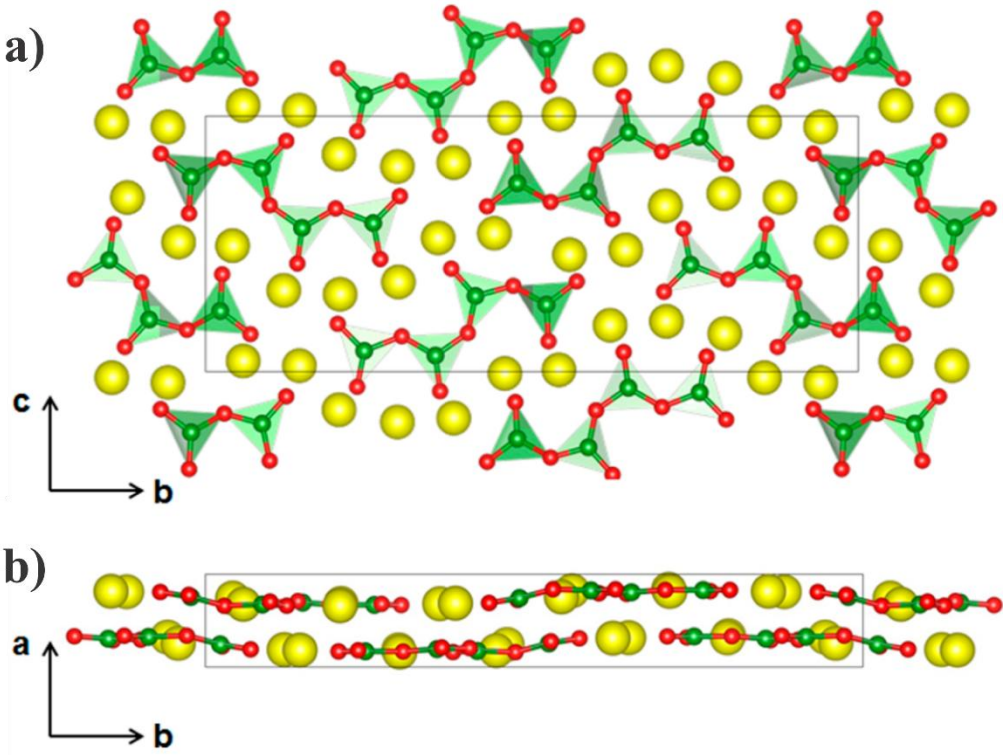

Figure 4.5 The structure of $Li_6B_4O_9$, when viewed along the [100] a) and [001] b) crystallographic axes, shows B, O, and Li atoms represented in green, red, and yellow, respectively. The BO_3 triangular units are also depicted in green, highlighting the arrangement of boron and oxygen atoms within the lattice structure.

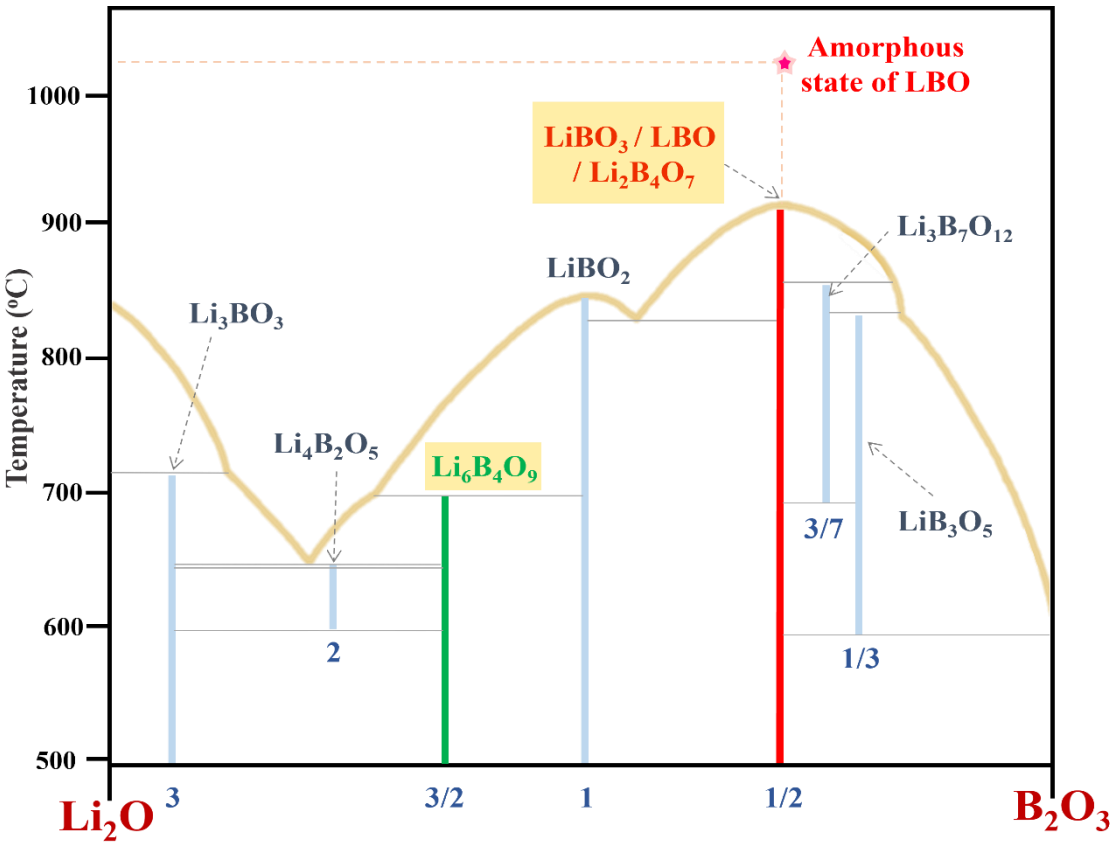

Figure 4.6 The binary phase diagram of Li_2O–B_2O_3, adapted from reference (G. l. Rousse et al., 2014).

The Li_2O–B_2O_3 binary system, which has been studied for over 50 years, exhibits significant complexity with around 10 distinct compounds, some of which are high-temperature or pressure-induced polymorphs (Figure 4.6). In ceramic production, solid-state reactions are often favored over soft chemical routes due to their cost-effectiveness and scalability (G. l. Rousse et al., 2014). However, sourcing B_2O_3 for borate production poses challenges. Both H_3BO_3 and B_2O_3 were initially used, but issues such as the loss of B_2O_3 through volatilization and solubility in aqueous environments led to complications, including the formation of $Li_4B_2O_5$. To compensate for this, excess B_2O_3 was added, which ultimately resulted in lithium metaborate ($LiBO_2$) formation. $LiBO_2$ has proven to be a stable and suitable starting material for synthesizing $Li_6B_4O_9$ when reacted with Li_2CO_3. according to the following equation:

$$4LiBO_2 + Li_2CO_3 \longrightarrow Li_6B_4O_9 + CO_2 \qquad \text{Equation 4.2}$$

Successfully forms $Li_6B_4O_9$ ceramics when sintered at 600°C, as confirmed by XRD traces showing no secondary phases. Full density is achieved near 630°C, suggesting $LiBO_2$'s superiority over other borate sources like H_3BO_3 and B_2O_3. The crystal structures of compounds within the Li_2O–B_2O_3 system have been thoroughly investigated, with six lithium borate crystals synthesized and characterized, including $Li_6B_4O_9$ (Zhou et al., 2018).

The incorporation of V_2O_5 into the glass system facilitates the bonding between boron and vanadium, leading to the formation of a glass matrix. Several studies have reported that in Li_2O– V_2O_5–B_2O_3 glass systems, increasing the V content significantly enhances the bonding between vanadium and boron (Saetova, Raskovalov, Antonov, Denisova, and Zhuravlev, 2020; Saetova et al., 2018). This finding has also been corroborated by molecular dynamics simulations, further confirming the strengthening of these interactions as V content increases. Meanwhile, the amount of Li_2O remains unchanged, but the B_2O_3 content decreases due to its reaction with vanadium. Consequently, the remaining ratio of Li_2O to B_2O_3 is 3:2 (Lelong et al., 2017). According to the binary phase diagram (Figure 3a), this ratio at approximately 700°C results in the formation of LiB_4O_9. This finding is consistent with the peaks observed in the $[[NC41]_m$ $+V]_m$ and $[NCV41]_m$ samples (Figure 4.3).

From the experimental data, a phase diagram of the melt quenching process was simulated as shown in Figure 4.7a-b. In Figure 4.6, it is evident that the research employed a temperature of 1100°C for the crystallization process, followed by rapid cooling to prevent crystallization, resulting in an amorphous structure in the glass, as seen in samples like LBO and $[NC41]_m$ (Figure 4.7b). This outcome aligns with the binary phase diagram, which indicates that rapid cooling leads to the formation of an amorphous structure.

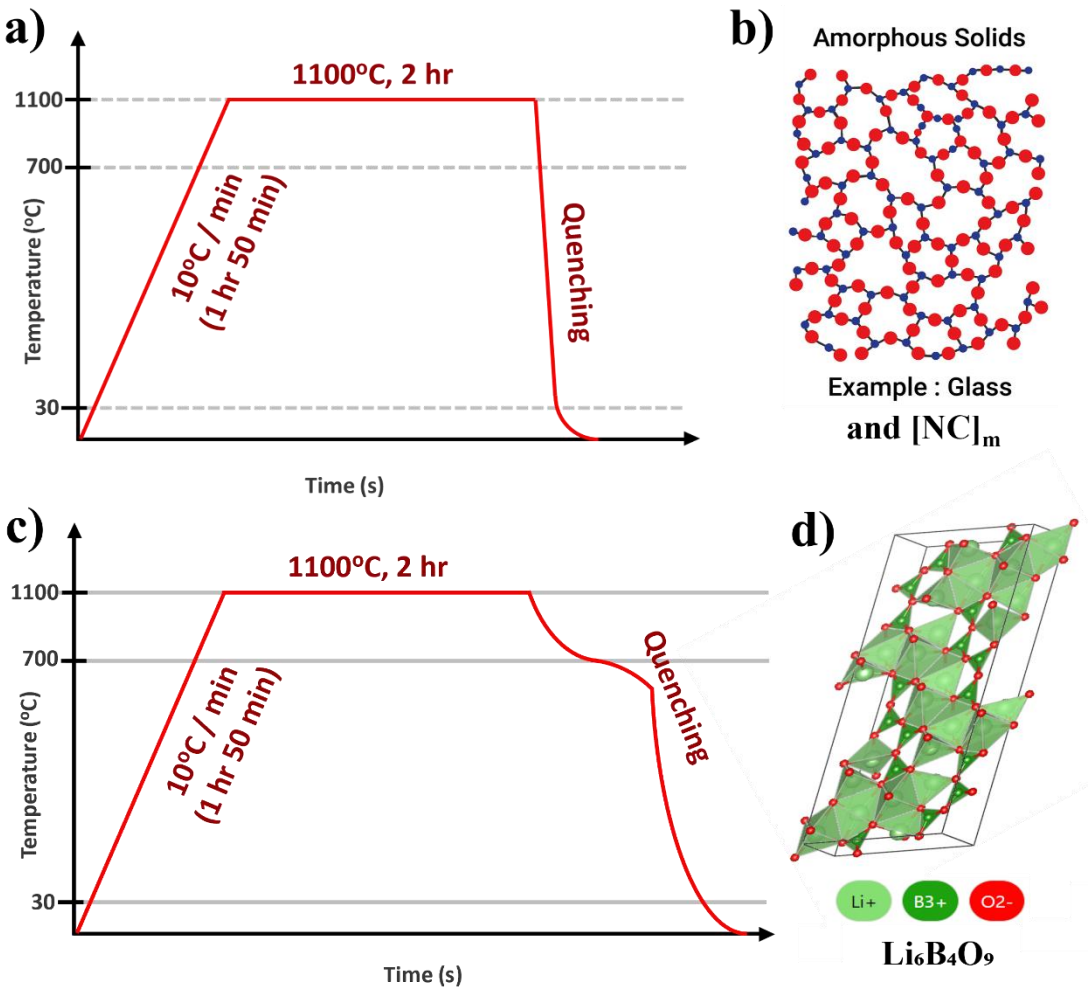

Figure 4.7 Schematic diagram of the melting process steps.

The formation of the glass-ceramic structure of $Li_6B_4O_9$, as illustrated in Figure 4.7c-d, involves a melt-quenching process. In step (Figure 4.7a) of this process, LBO is first melted and then rapidly cooled to create a disordered structure. This is followed by a melt quenching to induce partial crystallization, resulting in a material that exhibits ceramic-like. In this study, the sample underwent two firing steps consistent with the glass-ceramic formation process. Initially, the LBO glass base was prepared by melting at 1100°C and then quickly cooled. It was then combined with Ni, Co, and V_2O_5, followed by a second firing at the same temperature of 1100°C. This heat treatment encourages atoms to rearrange into a more ordered, crystalline structure, though some portions may remain in a glassy state. Previous studies have indicated that the addition

of a significant amount of vanadium (75%) can slow the cooling process, as depicted in the cooling diagram in Figure 4.7b. The low sintering temperature of $Li_6B_4O_9$ ceramic (Figure 4.7d), approximately 700°C, allows for atomic movement and realignment within the glass, ultimately leading to the formation of a crystalline structure.

4.3 Battery capacity measurement

Battery capacity measurement is a crucial process for assessing the performance and efficiency of batteries. The capacity of a battery is measured in ampere-hours (Ah) or milliampere-hours (mAh). The process involves fully charging the battery to a specified voltage, followed by discharging it continuously until the voltage drops to a predetermined level. The capacity is calculated based on the amount of current discharged over this period. This measurement can be conducted through controlled charging and discharging conditions. Accurate battery capacity measurement is essential for evaluating the battery's ability to store and deliver energy.

C-rate or Charge Rate is an indicator of the charging or discharging rate of a battery in relation to its full capacity. The C-rate value shows how fast the battery can be charged or discharged compared to its full capacity. For example, a C-rate of 1C means the battery can be fully charged or discharged in 1 hour, while a C-rate of 0.5C means it will take 2 hours to charge or discharge the battery fully. A lower C-rate results in a longer charging or discharging time. Selecting an appropriate C-rate helps to extend the battery's lifespan and maintain its performance over the long term.

$$C\text{-rate}=QI \qquad \text{Equation 4.3}$$

In this study, a C-rate of 0.2 Ah/g was used, meaning that charging or discharging took place over 5 hours. This value was determined experimentally to achieve optimal performance. From the equation, the current used for charging or discharging was calculated to be 0.04 A/g. The average weight of each sample used in the anode substrate was 8.64 mg (All substrate). To determine the mass of the active material in each sample (Total mass), the formula (Total mass - All substrate) * 0.8 was applied,

where the factor of 0.8 accounts for the presence of carbon black (CB) along with the active material. Once the mass of the active material was obtained, the current was divided by the mass to calculate the starting and ending current required for the experiment.

Setting the voltage range in battery testing is a critical step that impacts the accuracy and reliability of measurements. Setting the voltage range too low may result in missing important data and an inability to accurately observe differences in low battery voltages. Conversely, setting the voltage range too high can lead to damage or risk of damage to the battery. Considering the appropriate voltage range for testing is crucial to obtain accurate and trustworthy results. It also helps prevent potential damage to the battery from testing with inappropriate voltage levels.

In some samples, the voltage range is adjusted due to the low charge and conductivity of LBO, which necessitates the use of a lower voltage range to improve its electrical conductivity. In this study, a voltage range of 0.2–2V was used for LBO. In contrast, V_2O_5 was set to operate within the 2–4V range due to its suitable electrical properties and behavior in this voltage range. The 2–4V range is crucial for V_2O_5 in several aspects, such as structural stability, electrical performance, and redox reactions, involving changes in oxidation states between V^{5+} and V^{3+}, allowing for efficient energy storage and release. Moreover, this voltage range enables V_2O_5 to work synergistically with other materials in lithium-ion batteries, enhancing overall battery performance.

For the other samples, the capacity values are illustrated in Figure 4, and the summarized data are presented in Table 4.2. This table compares the samples using the average values from cycles 1 to 100 for calculating specific capacity, energy density, and capacity retention. The data reveal that the $[NC41]_m$ sample, used as the cathode, exhibited the highest specific capacity in the first cycle. However, as the number of cycles increased, the capacity decreased rapidly. This phenomenon is attributed to the Initial Coulombic Efficiency (ICE), which is the ratio of the energy a battery can discharge in the first cycle compared to the energy it was charged with. ICE is typically lower

than the charged energy due to factors such as energy loss during charging and discharging, the formation of a protective Solid Electrolyte Interphase (SEI) layer on the electrode surface, and heat loss. This SEI layer, which forms during the first cycle, consumes some lithium ions, thereby reducing the battery's capacity to discharge energy in subsequent cycles (He, Sun, Tang, Wang, and Shao, 2019). For this work, we excluded the first cycle and designated the second cycle as the new first cycle. As for the 99^{th} cycle, it represents the 100^{th} cycle.

In the battery testing, coin cells were assembled following the procedures mentioned earlier. The voltage range was appropriately set for each sample material: 0.2-2V for LBO, 0.5-3V for $[NC41]_m$ and 2-4V for samples containing V_2O_5. These voltage ranges were selected based on the suitability of the materials' properties and electrical behavior within these ranges.

The specific capacity compared to the number of cycles (Cycle Test) from 1 to 100 cycles, as shown in Figure 4a, revealed that LBO had an average capacity of 11.81 mAh/g (average from cycles 5 to 100) and an energy density of 272.01 mWh/g, which is relatively low. However, its capacity was notably stable, consistent with reports on LBO's stability, such as the study by (Siriroj et al., 2022), which found that the battery maintained 99.28% of its capacity after numerous cycles, indicating a loss of only 0.72% from its initial capacity. Meanwhile, the battery using V_2O_5 as the cathode delivered approximately 224.33 mAh/g and had an energy density of about 653.14 mWh/g, which is relatively high. However, the battery maintained only 78.57% of its initial capacity after 100 cycles, indicating a 21.43% reduction in capacity retention. Data from Figure 4a showed a significant decrease in the capacity retention of V_2O_5 over the number of cycles, which is a natural property of V_2O_5. The vanadium oxide structure in this material is fragile and prone to degradation after repeated use, leading to a rapid decrease in battery capacity (Cheah, Aravindan, and Madhavi, 2013; Li et al., 2021).

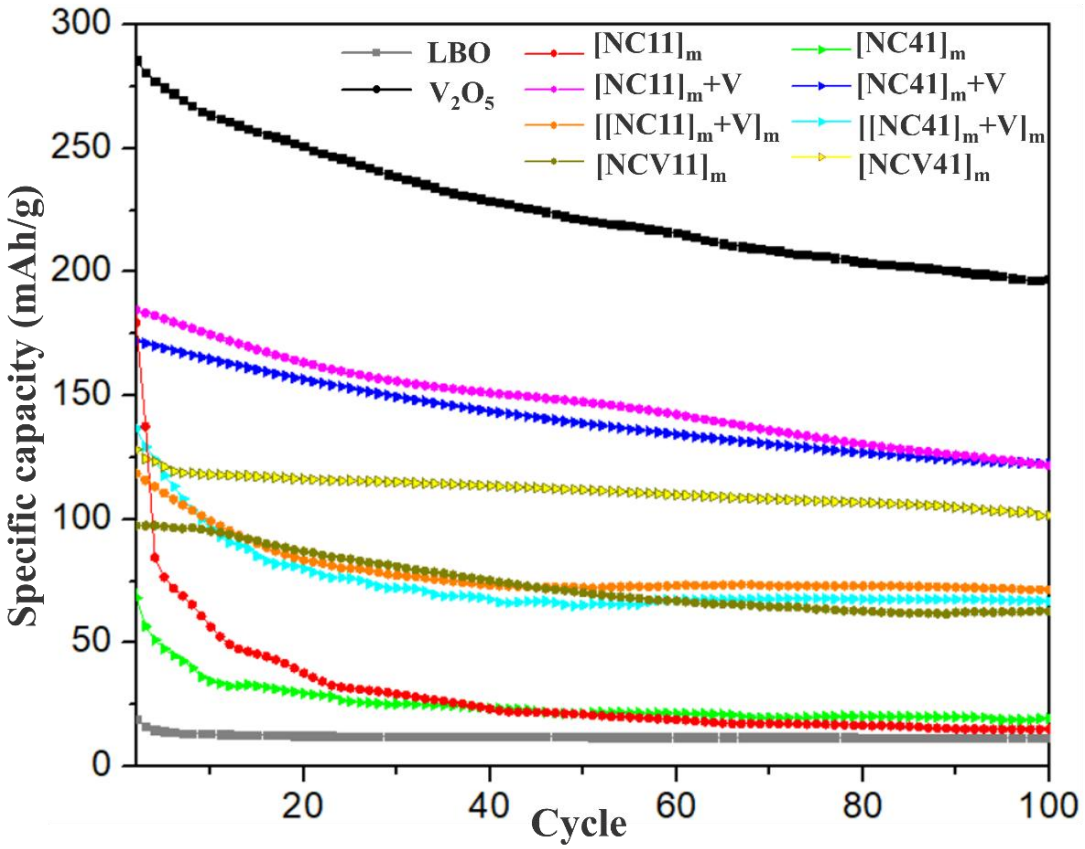

Figure 4.8 Specific capacity as a function of the number of cycles.

In the $[NC41]_m$ sample, the average specific capacity and energy density were the lowest, with values of 24.09 mAh/g and 20.55 mWh/g, respectively. Additionally, the capacity retention was 65.54%, which is also the lowest among the samples. This indicates that the combination of LBO with Ni:Co in a 4:1 ratio, followed by the melting process, resulted in an increase in capacity compared to pure LBO, with an increase of approximately twofold or around 54%. Moreover, the sample also exhibited stability in accordance with the properties of LBO. In the case of the $[NC11]_m$ sample, the average specific capacity and energy density were the lowest, with values of 24.09 mAh/g and 20.55 mWh/g, respectively. Additionally, the capacity retention was 65.54%. Over time, while the capacity remained relatively stable, the specific capacity was still quite low.

Table 4.2 Illustrates the Specific capacity (mWh/g) and Energy density (mAh/g) along with the Capacity Retention (%).

Sample	Specific capacity (mAh/g)	Energy density (mWh/g)	Cycle 1	cycle 100	Capacity Retention (%)	Capacity Fade (%)
LBO	11.82	8.57	12.64	11.69	92.46	7.54
V_2O_5	226.31	658.97	283.51	196.48	69.30	30.70
$[NC11]_m$	29.25	19.90	96.004	15.08	15.71	84.29
$[NC11]_m$+V	147.33	430.02	161.96	125.61	77.56	22.44
$[NC11]_m$+V$]_m$	78.61	219.45	118.39	71.27	60.20	39.80
$[NC11+V]_m$	74.01	201.45	102.26	62.69	61.31	38.69
$[NC41]_m$	25.19	21.46	68.18	19.26	28.25	71.75
$[NC41]_m$+V	141.26	414.58	174.26	122.94	70.55	29.45
$[NC41]_m$+V$]_m$	74.17	207.27	142.26	66.94	47.06	52.94
$[NC41+V]_m$	111.42	306.26	130.43	105.24	80.69	19.31

The experimental results of the samples mixed with 75% V_2O_5 revealed that the sample $[NC11]_m$ +V (Figure 4.8) had an average capacity of approximately 59.85 mAh/g (average from 1-100 cycles) and an energy density of 169.00 mWh/g, with a capacity retention of 62.06%. The $[NC41]_m$ +V sample showed the highest capacity and energy density at 140.13 mAh/g and 410.93 mWh/g, respectively. The observed capacity values are relatively high, yet the stability remains suboptimal.

The samples that were mixed with 75% V_2O_5 and subjected to the melt quenching process had different results. The $[[NC11]_m +V]_m$ lt sample had an average capacity and energy density of around 77.05 mAh/g and 215.90 mWh/g, with a capacity retention of 87.36%, indicating a capacity loss of only 12.64% over 100 continuous cycles. Meanwhile, the $[[NC41]_m +V]_m$ sample had an average capacity of 72.36 mAh/g and an energy density of 202.04 mWh/g, which aligns with previous reports (Siriroj et al., 2023; Siriroj et al., 2022), and a capacity retention of 85.05%, showing a capacity loss of only 14.95% after 100 cycles. The observed capacity, while measurable, remains below the desired level and exhibits stability that is not yet satisfactory. Further optimization is required to enhance both the capacity and stability to meet the expected performance standards.

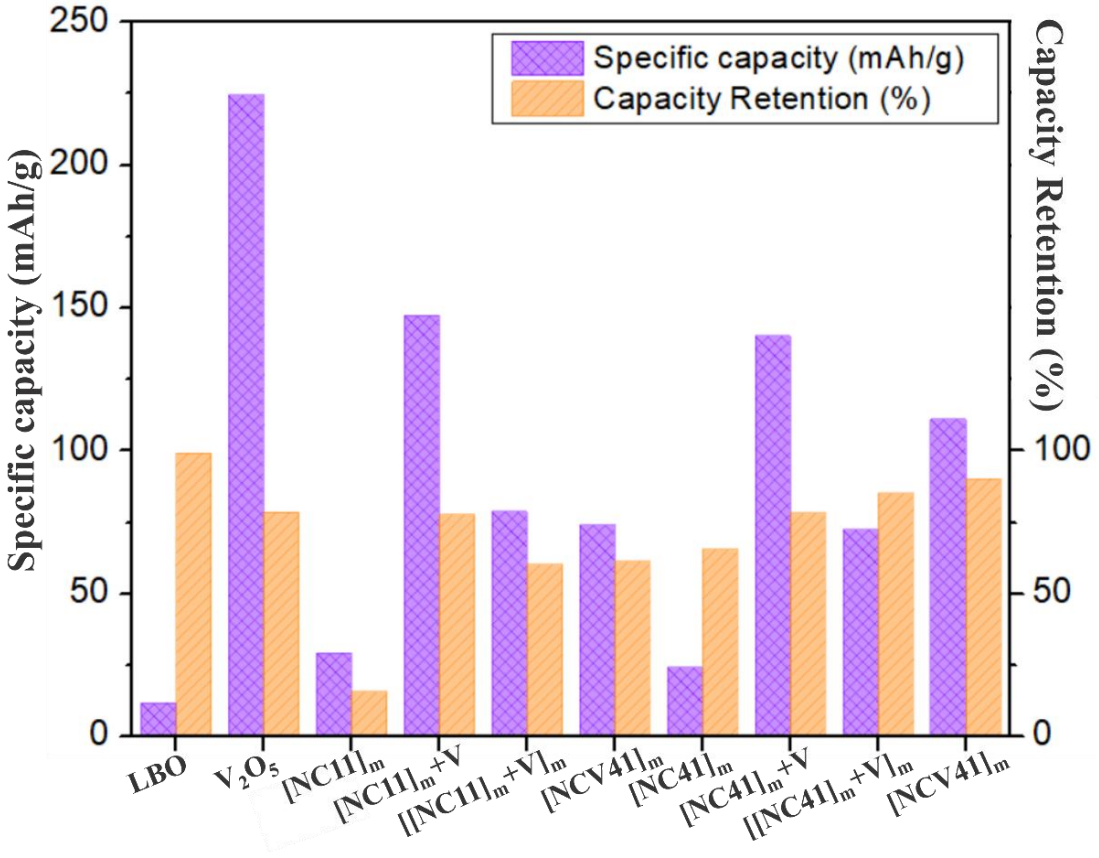

Figure 4.9 Comparison of Specific capacity and Capacity retention in average cycle test of 1 to 100 cycles.

For the samples where LBO, Ni, Co, and V_2O_5 were mixed through the melt quenching process, the $[NCV11]_m$ sample showed an average capacity of around 71.97 mAh/g and an energy density of 198.64 mWh/g. The calculated capacity retention was 79.47%, meaning a capacity reduction of only 20.53% after 100 cycles. The $[NCV41]_m$ sample exhibited an average capacity of 110.96 mAh/g and an energy density of 304.80 mWh/g, with a capacity retention of 90.27%, showing only a 9.73% capacity loss after 100 continuous cycles. The $[NCV41]_m$ sample demonstrated a notably high capacity, which is highly satisfactory. Moreover, it exhibited excellent stability throughout testing. In addition to its promising performance, the fabrication process of this sample is straightforward and uncomplicated, further enhancing its practicality for application.

For all four samples, an additional firing process was applied, which caused significant capacity reduction, as shown in Figure 4.8. This was due to the formation of a glass-ceramic structure of $Li_6B_4O_9$ during the firing process, as displayed in Figure 4.3, which revealed a hexaborate structure. This structure enhances strength and durability, allowing the material to withstand long-term use in harsh conditions requiring high strength and damage resistance (Cahill and Graeve, 2019).

4.4 The electrochemical properties by charge and discharge curve

In batteries, the electrochemical properties are evaluated using charge and discharge curves. These curves are crucial for testing various performance aspects, such as capacity, voltage stability, and overall energy efficiency during cycling. By analyzing the charge and discharge profiles, researchers can assess the battery's ability to store and release energy, monitor the voltage changes at different states of charge, and identify any potential degradation in performance over time. This method provides valuable insights into the battery's behavior under real-world operating conditions.

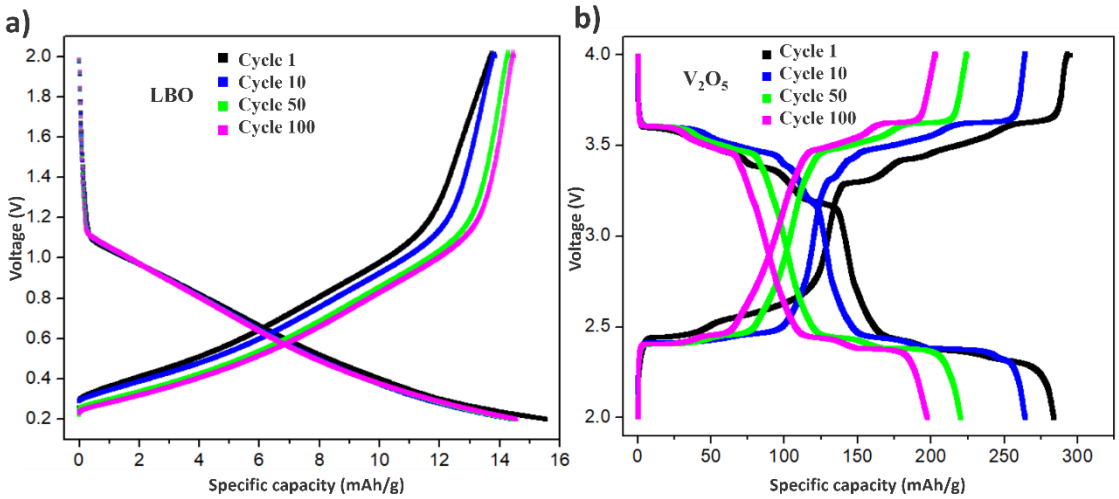

Figure 4.10 The voltage-capacity curves for charge and discharge cycles of a) LBO and b) V_2O_5 at the 1st, 10th, 50th, and 100th cycles.

The results of the charge and discharge curve also revealed that LBO exhibited better voltage stability and overall energy efficiency during cycling compared to V_2O_5. LBO (Figure 4.10a) maintained a consistent voltage throughout the charge-discharge process, contributing to its stable performance over time. In contrast, V_2O_5 (Figure 4.10b) showed significant voltage fluctuations during charging states, indicating instability in its electrochemical behavior. Additionally, V_2O_5 experienced noticeable degradation in performance over time, with a reduction in capacity retention, highlighting its vulnerability to structural breakdown after prolonged use.

Figure 4.11 presents the charge and discharge cycles at the 1st, 10th, 50th, and 100th cycles. From the figure, it is evident that a) $[NC11]_m$ and b) $[NC11]_m$ +V show significant changes as the number of cycles reaches 100, indicating a decline in performance. In contrast, c) $[[NC11]_m$ +V$]_m$ and d) $[NCV11]_m$ exhibit improved stability in voltage and overall energy efficiency throughout the cycling process, demonstrating better performance and consistency over time.

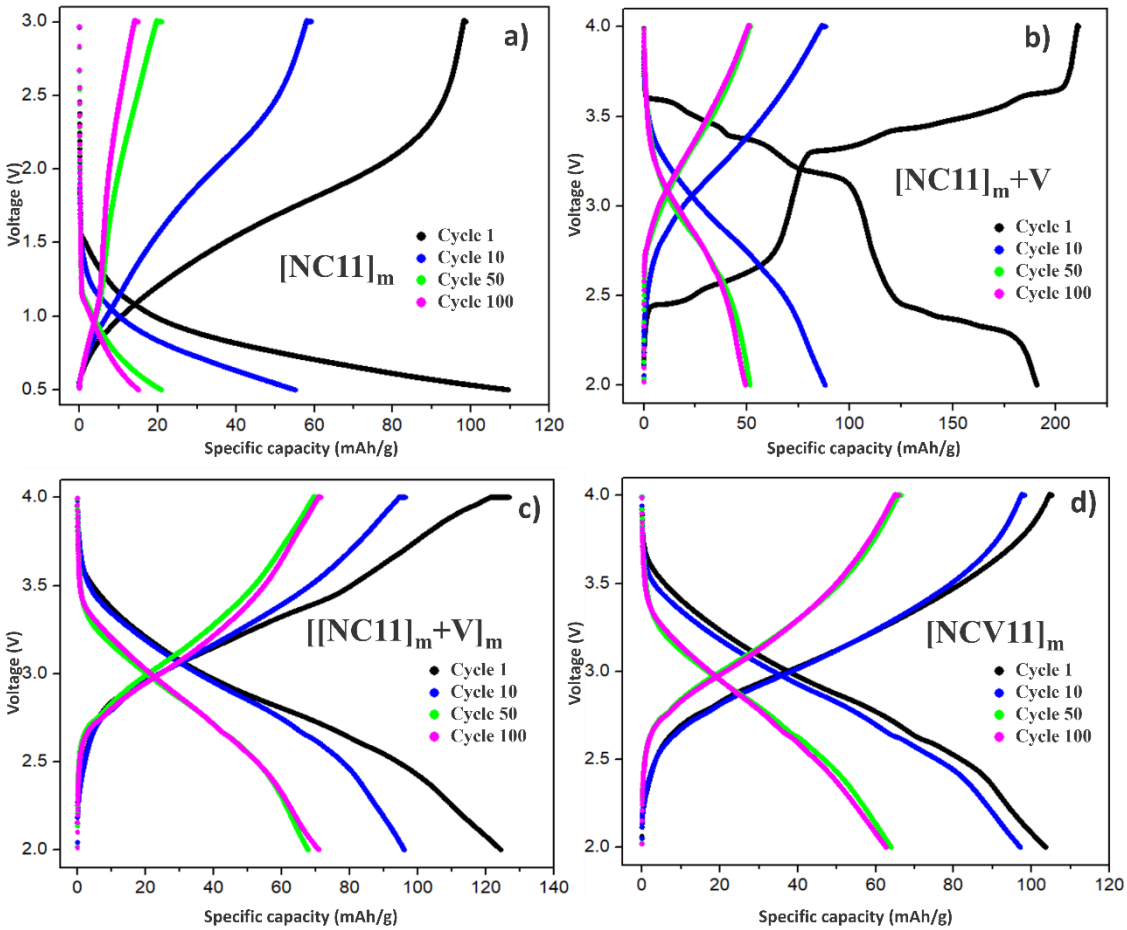

Figure 4.11 The voltage-capacity curves for charge and discharge cycles of a) $[NC11]_m$, b) $[NC11]_m$ +V, c) $[[NC11]_m$ +V$]_m$, and d) $[NCV11]_m$ at the 1st, 10th, 50th, and 100th cycles.

Figure 4.12 illustrates the charge and discharge profiles at the 1st, 10th, 50th, and 100th cycles. The results reveal noticeable degradation in performance for samples a) $[NC41]_m$, b) $[NC41]_m$ + V, and c) $[[NC11]_m$ + V$]_m$ by the 100th cycle. Conversely, sample d) $[NCV4\ 1]_m$ showed enhanced stability in both voltage and energy efficiency, maintaining more consistent performance throughout the cycling process.

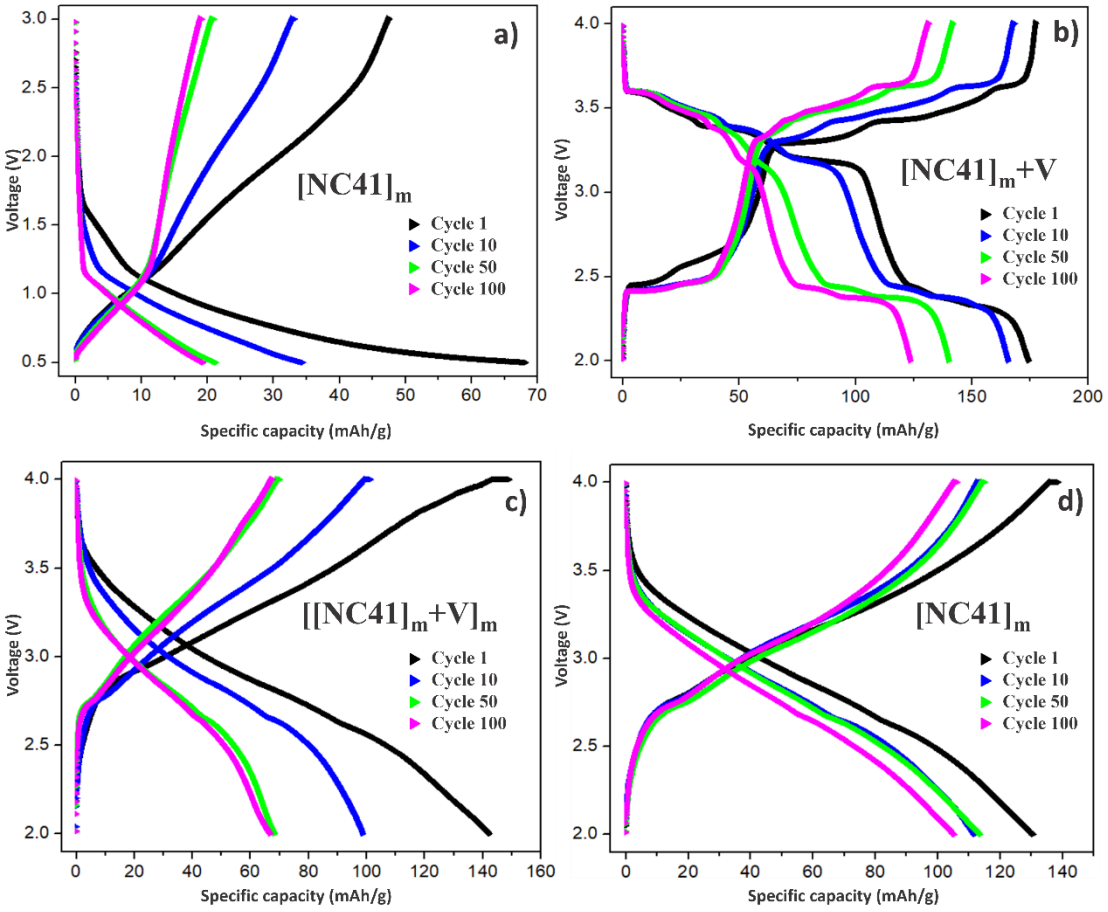

Figure 4.12 The voltage-capacity curves for charge and discharge cycles of a) $[NC11]_m$, b) $[NC11]_m$ +V, c) $[[NC11]_m$ +V$]_m$, and d) $[NCV11]_m$ at the 1st, 10th, 50th, and 100th cycles.

4.5 The Electrochemical Impedance Spectroscopy (EIS) technique was employed to determine impedance values within the battery electrodes

The study utilized Electrochemical Impedance Spectroscopy (EIS) to assess the impedance values of the battery electrodes. This technique provided valuable insights into the internal resistance and charge transfer properties of the materials, helping to evaluate their overall electrochemical performance. The EIS analysis allowed for a deeper understanding of the conductivity and resistance characteristics, which are crucial factors for optimizing battery efficiency and longevity.

To gain further insights, cyclic voltammetry (CV) and electrochemical impedance spectroscopy (EIS) measurements were conducted. A new set of cells was used, with EIS measurements taken first, followed by three cycles of CV, and a final EIS measurement. The CV measurements began from the open-circuit voltage of the cells, which was approximately 2.5 V, and were performed at a scan rate of 0.5 mV/s.

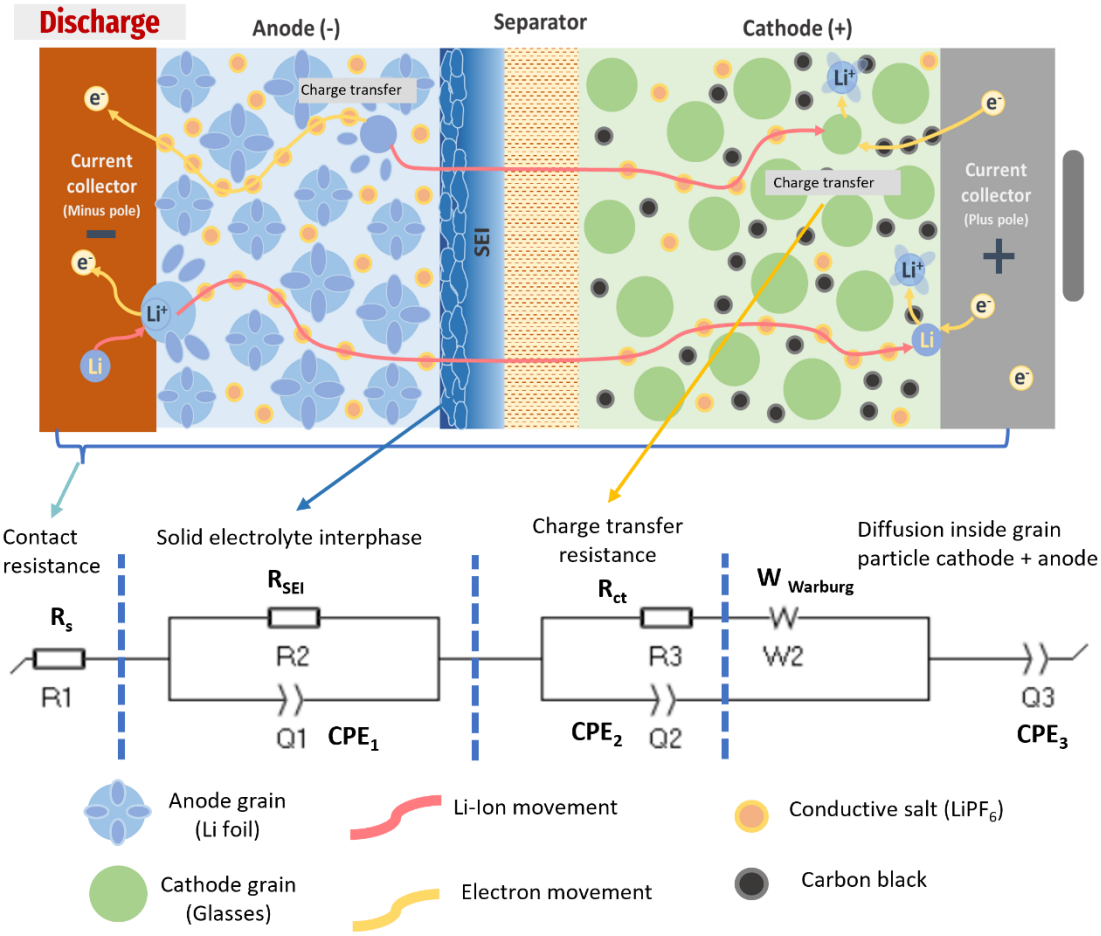

Figure 4.13 The movement of ions and electrons during discharge was examined using a lithium-ion battery with a lithium foil anode and a glassy carbon cathode as an example.

The internal changes within the cell during testing were evaluated by conducting EIS measurements before and after the test. The EIS results, presented in Figure 4.14, were analyzed by fitting the data to the model shown in Figure 4.13.

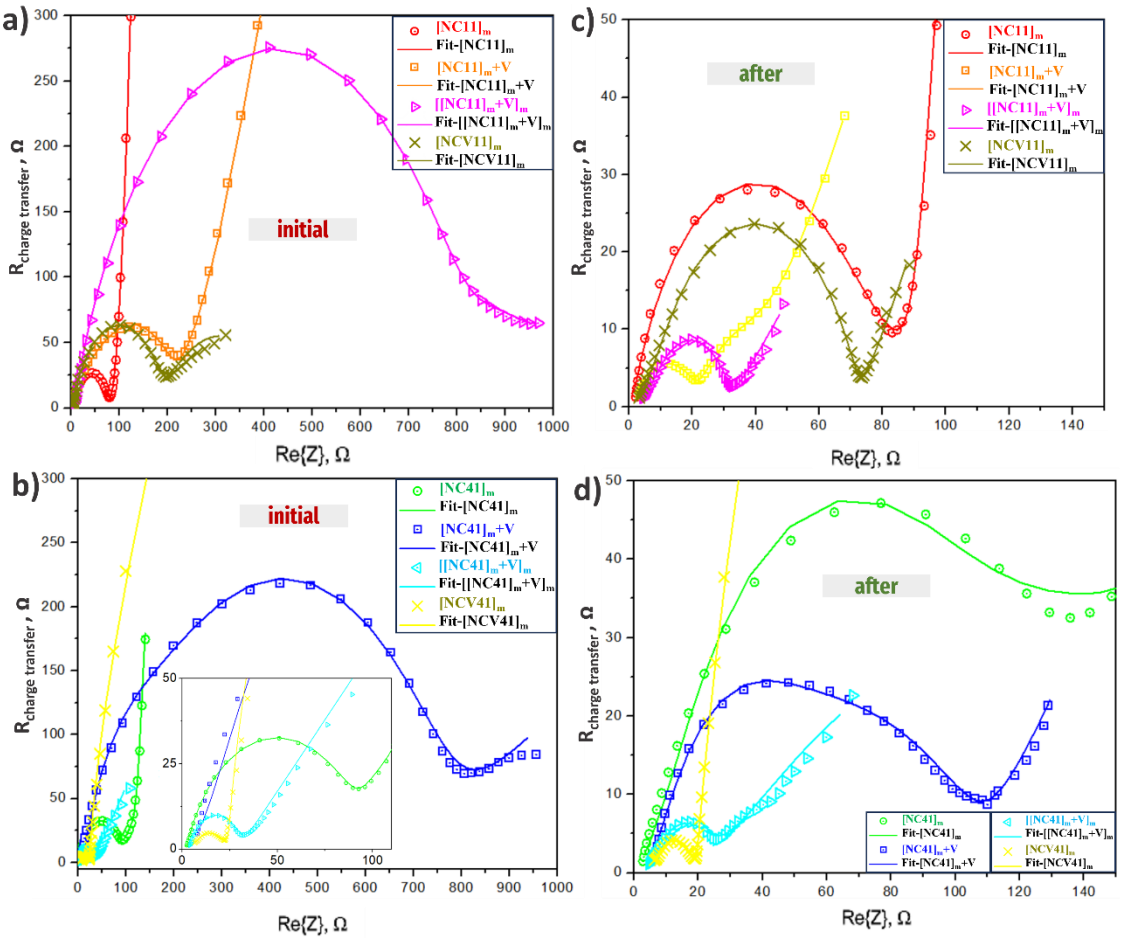

Figure 4.14 c) The initial cell assembly and d) the condition after three cycles of CV testing were analyzed using EIS measurements.

The charge transfer resistance, which reflects ion transfer within the cathode, was examined for the $[NC11]_m$ and $[NC41]_m$ sample. It was found that the internal resistance before measurement and after three cycles of CV (Figures 4.14a-d) did not differ significantly. In contrast, the $[NC11]_m$ +V and $[NC41]_m$ +V sample exhibited a high initial internal resistance, reaching up to 600-800 **Ω**. This elevated resistance is attributed to

the low ionic conductivity of the LBO glass and V_2O_5, which contributed to the increased internal resistance of the cell. However, after CV testing, a subsequent EIS measurement revealed that the resistance decreased to 20-80 Ω, though it still remains relatively high.

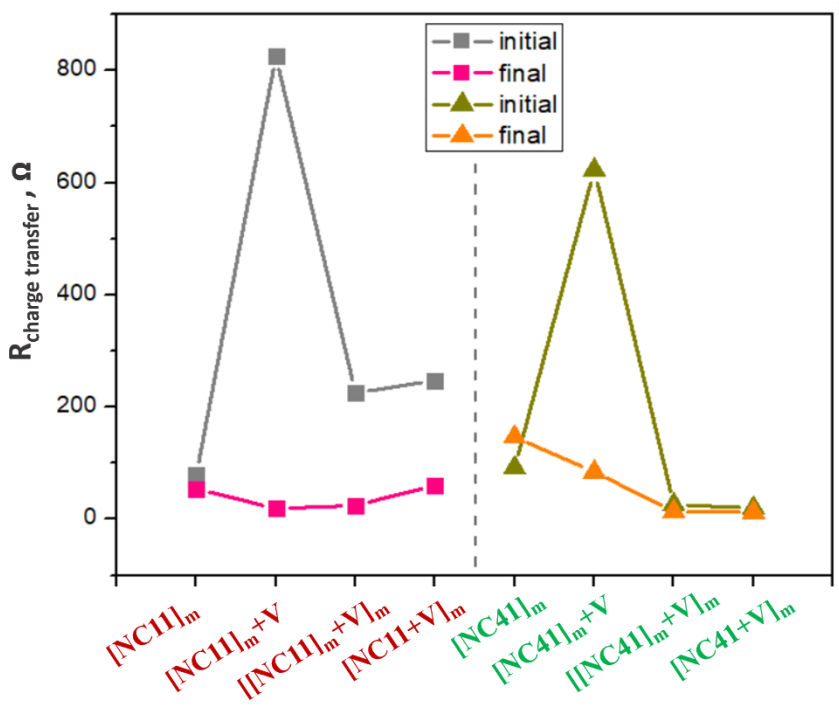

Figure 4.15 EIS measurements were compared initially and after testing.

In the samples of $[[NC11]_m +V]_m$, $[[NC41]_m +V]_m$, $[NCV11]_m$ and $[NCV41]_m$, the internal resistance values remained remarkably stable before and after measurement, with only a slight reduction observed following three cycles of CV testing. This stability is a clear indication that the incorporation of V_2O_5, followed by melt-quenching process, significantly strengthens the material's structure and enhances its durability. The consistency in resistance reflects the superior atomic arrangement and molecular bonding, which contribute to the material's remarkable resilience under stress (Cahill and Graeve, 2019). Such advanced resistive properties are crucial in minimizing energy loss within the battery, ultimately leading to enhanced performance and significantly extending the battery's lifespan. This promising outcome aligns perfectly with earlier

experimental findings, underscoring the material's potential for high-efficiency, long-lasting energy storage solutions.

4.6 The specific capacitance measurements of glass electrodes using cyclic voltammetry (CV).

The specific capacitance of the glass electrodes was evaluated using cyclic voltammetry (CV) measurements. This method provided insights into the electrochemical behavior of the electrodes, revealing any potential phase transitions during the testing process. Changes in the shape of the CV curves, especially at different scan rates, offered valuable information about phase transitions occurring within the glass materials, helping to assess their electrochemical stability and overall performance.

Additional insights from CV measurements were obtained using the same cell as the EIS measurements. EIS was measured first, followed by two CV cycles. The CV measurements started from the open-circuit potential of the cell, which was approximately 2.5 V, and the potential was swept between 2.0 V and 4.0 V at a scan rate of 0.5 mV/s. The results from the third CV cycle are shown in Figure 4.16, where (a and c) represents the Ni: Co ratio of 1:1 and (b and d) the Ni: Co ratio of 4:1. Here's the corrected version:

The CV graph represents the relationship between current density, which refers to the amount of electric current flowing through the electrode in an electrochemical system, and potential (V vs Li/Li^+), which measures the voltage during the intercalation and deintercalation of lithium ions (Li^+) into/from the electrode materials in the battery system. In Figure 4.16-4.17, the comparison with V_2O_5 (black line) highlights the phase transitions occurring within different glass systems. The characteristics of V_2O_5 exhibit well-defined redox peaks, indicating the intercalation of Li-ions into the material. One Li-ion intercalation process occurs between 3.0 and 3.5 V versus Li/Li^+. In the first three cycles shown in Figure 4.16-4.17, the 3^{th} cycle (Figure 4.18-4.19) clearly displays three

cathodic peaks at 3.31 V, 3.13 V, and 2.23 V, corresponding to the cathodic process of a redox reaction. This refers to the process occurring at the cathode of an electrochemical cell during reduction, involving electron acceptance and comprising three distinct steps.

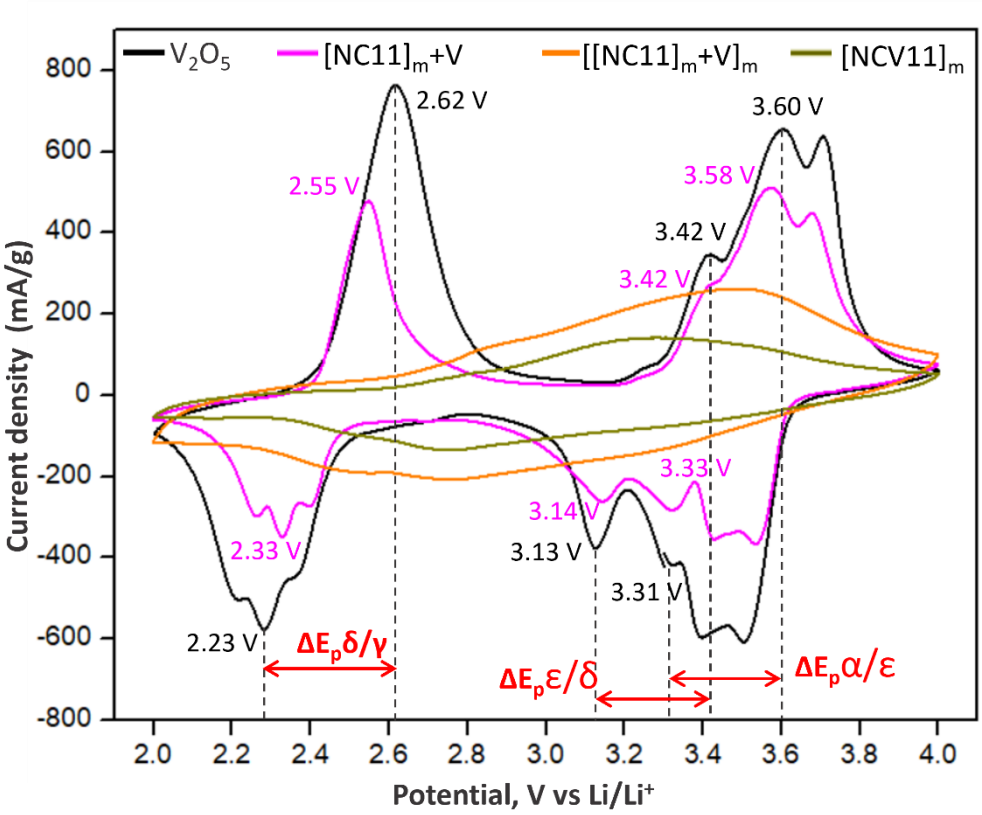

Figure 4.16 The coin cells with glass samples underwent three cycles of EIS measurements, followed by CV testing. The redox peak separation (ΔEp) for the third cycle of V_2O_5, $[NC11]_m$ +V, $[[NC11]_m+V]_m$ and $[NCV11]_m$.

The first process involves the crystal phase transition from **α/ε** (αV_2O_5 to **ε**-$Li0.5V_2O_5$). αV_2O_5, or alpha-phase vanadium pentoxide, is the initial crystal structure of V_2O_5 in its stable **α**-phase. **ε**-$Li0.5V_2O_5$, or epsilon-phase lithium vanadium pentoxide, forms when lithium ions are intercalated into the structure of **α**-V_2O_5,

causing a change in the crystal structure to the ε-phase. In this phase, lithium ions are intercalated at a ratio of 0.5 lithium per V_2O_5.

The second process is the crystal phase transition from ε/δ (ε-LiV_2O_5 to δ-LiV_2O_5). In the epsilon-phase, lithium ions intercalate into the V_2O_5 structure at a ratio of 0.5 lithium per V_2O_5. δ-LiV_2O_5, or delta-phase, forms when additional lithium is inserted, reaching a ratio of 1 lithium per V_2O_5. The δ-phase is generally more stable and can accommodate more lithium ions compared to the ε-phase.

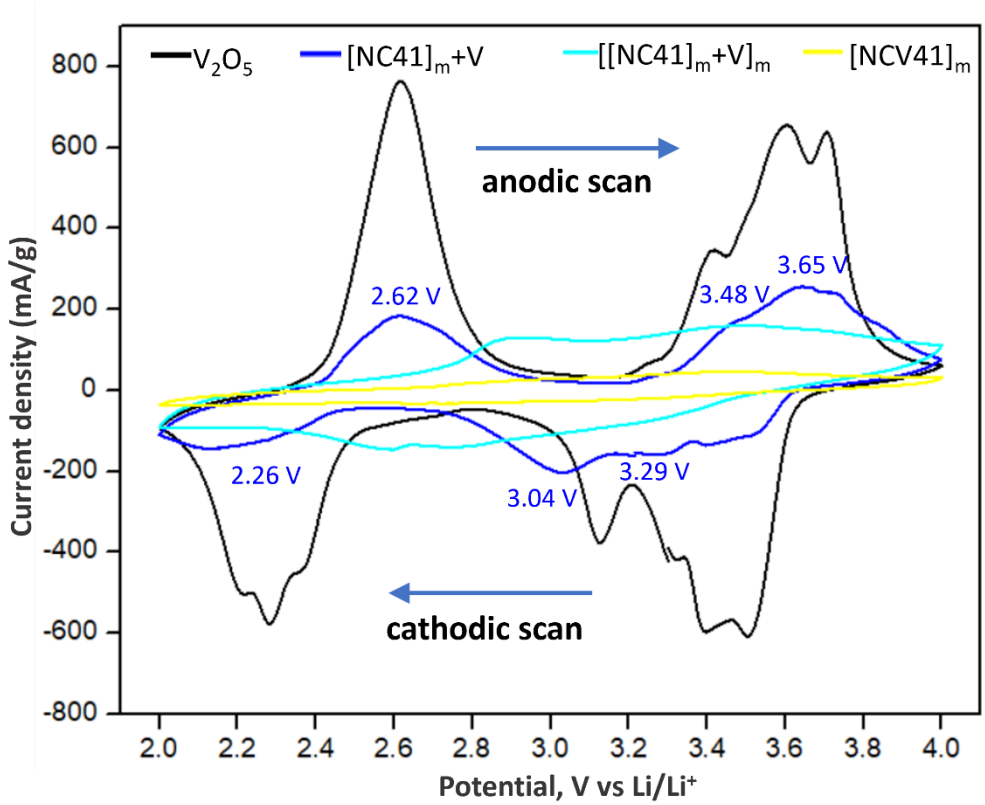

Figure 4.17 The redox peak separation (ΔEp) for the third cycle of $[NC41]_m$ +V, $[[NC41]_m$ +V$]_m$ and $[NCV41]_m$.

The third and final cathodic process is the δ/γ transition (δ-LiV_2O_5 to γ-$Li_2V_2O_5$), which refers to the crystal phase transition from the delta-phase to the gamma-phase. γ-$Li_2V_2O_5$, or gamma-phase, occurs when further lithium ions are intercalated, reaching a ratio of 2 lithium ions per V_2O_5. This phase change leads to the formation of the γ-

phase, which can support even more lithium ions than the δ-phase, resulting in higher capacity. However, this may also alter the structure compared to the previous phase (Armer et al., 2018; Wang, Chen, Xu, Wang, and Zhen, 2017).

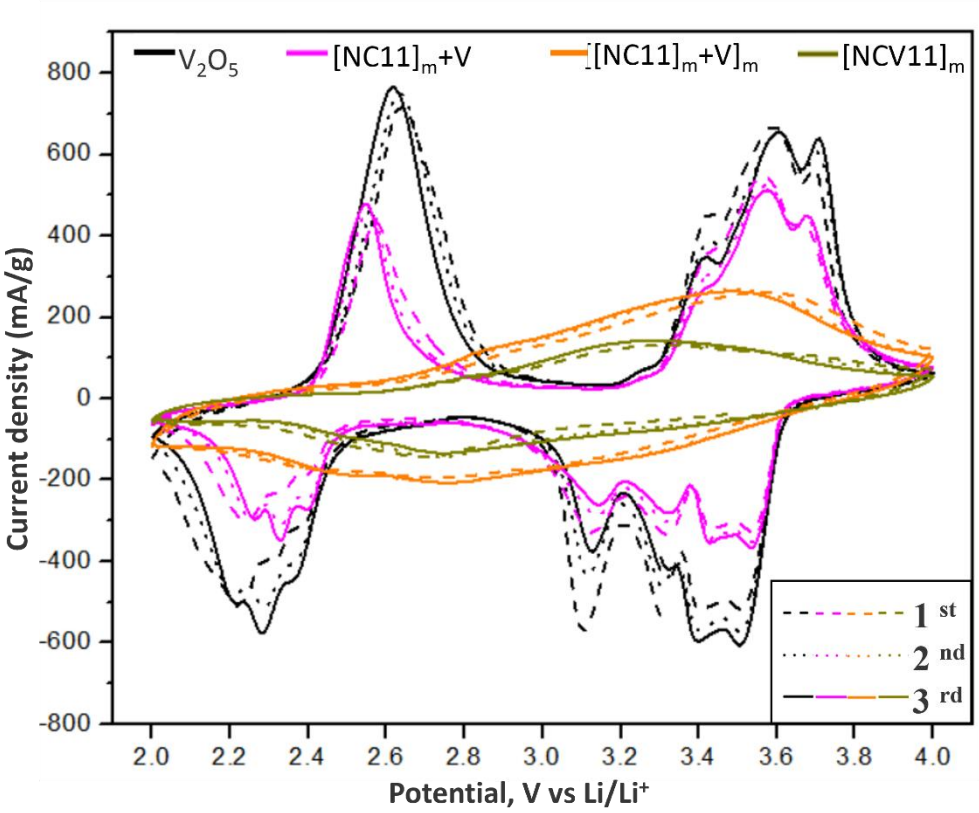

Figure 4.18 The graph displays CV data from the first to third cycles of V_2O_5, $[NC11]_m$ +V, $[[NC11]_m +V]_m$ and $[NCV11]_m$.

Simultaneously, three corresponding anodic peaks were observed at 2.62, 3.42, and 3.60 V, indicating the anodic process of the redox reactions on the anode. These peaks correspond to oxidation reactions occurring at the anode in the electrochemical cell, demonstrating good reversibility of the electrode. The separation of the redox peaks (ΔEp) for the α/ε, ε/δ, and δ/γ phase transitions in V_2O_5 were calculated to be 0.29, 0.29, and 0.39 V, respectively (Figure 4.16). A smaller potential difference suggests

more favorable Li^+ insertion/extraction reactions and highlights the importance of phase transition kinetics within the material.

In the $[NC11]_m$ +V sample, three distinct cathodic peaks were clearly observed at 3.33, 3.14, and 2.33 V, along with three anodic peaks at 3.58, 3.42, and 2.55 V. From Figure 4.18, the redox peak separations (ΔEp) for the **α/ε**, **ε/δ**, and **δ/γ** transitions in $[NC11]_m$ +V were calculated as 0.25, 0.28, and 0.22 V, respectively. For the $[NC41]_m$ +V sample, the redox peaks were less distinct, though three cathodic peaks were observed at 3.29, 3.04, and 2.26 V, and three anodic peaks at 3.65, 3.48, and 2.62 V. The redox peak separations (ΔEp) for $[NC41]_m$ +V were calculated as 0.36, 0.44, and 0.36 V, respectively, as shown in Figure 4.18.

For samples incorporating V_2O_5 into the glass system and then undergoing a subsequent firing process, no clear redox peaks corresponding to V_2O_5 were observed, as shown in Figure 4.16-4.17. However, a significant reduction in current density was noted. In batteries, lower current density implies reduced current flow through the energy storage system. The current density for $[[NC11]_m +V]_m$ was higher than $[NC11 +V]_m$, and similarly, the current density for $[[NC41]_m +V]_m$ was higher than $[NC41 +V]_m$, though V_2O_5 still exhibited the highest current density. This suggests that these four samples exhibited lower current flow through the energy storage material, possibly due to operation under low current load conditions. Adjusting the current to lower values helps conserve energy and prevents unnecessary energy loss during battery operation. Lower current density generally extends the battery's lifespan and enhances energy conservation during daily use, with $[NC11 +V]_m$ and $[NC41 +V]_m$ showing the lowest values, consistent with the CV results. Reducing the fluctuations in Li^+ insertion/extraction reactions within the material helps minimize energy loss during the battery's charge-discharge processes. This energy conservation also contributes to extending the battery's lifespan and maintaining capacity over the long term.

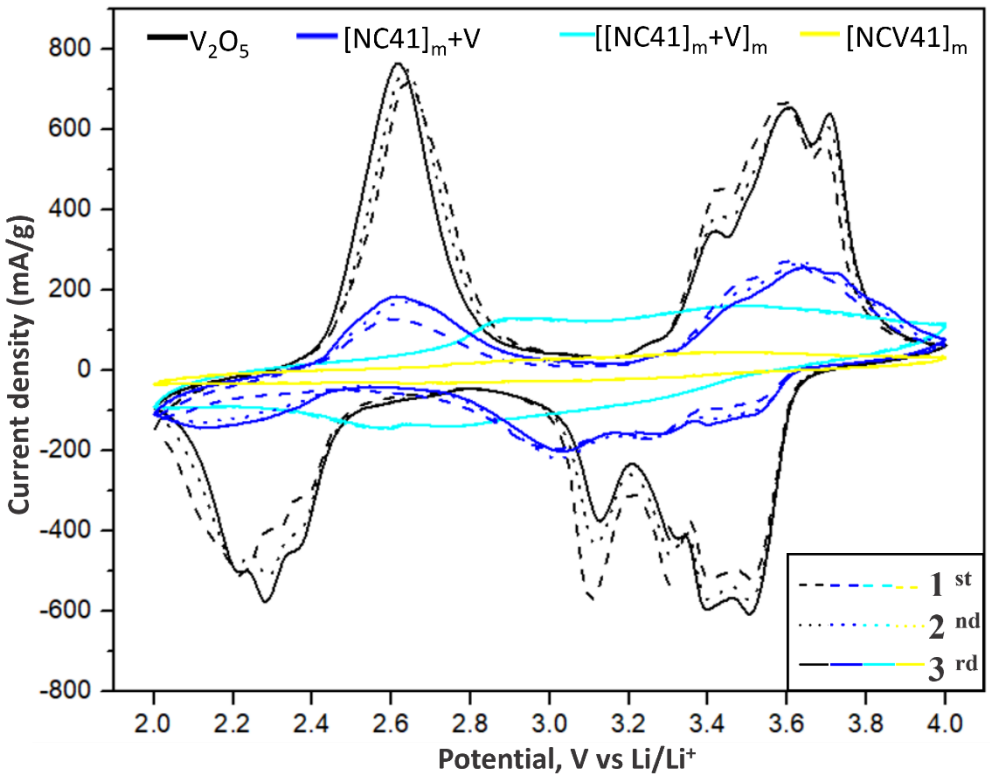

Figure 4.19 The graph displays CV data from the first to third cycles of V_2O_5, $[NC41]_m$ +V, $[[NC41]_m$ +V$]_m$ and $[NCV41]_m$.

Additionally, the CV curves in Figure 4.18-4.19 represent cycles 1 – 3 (excluding the initial cycle due to damaged initial graphs in each sample, which were not used for comparison). As shown, the curves for V_2O_5, $[NC11]_m$ +V, and $[NC41]_m$ +V in cycles 1, 2, and 3 exhibit noticeable changes in the CV profile and redox peak positions. However, for $[[NC11]_m$ +V$]_m$, $[[NC41]_m$ +V$]_m$, [NC11 +V$]_m$ and [NC41 +V$]_m$, as displayed in Figure 4.18-4.19. The curves nearly overlap from cycles 1 to 3 in terms of peak positions and intensities, indicating good stability and reversibility of the electrodes. This aligns with the battery capacity and Capacity Retention (%) measurements, emphasizing the importance of stability in maintaining battery performance over the long term. Materials that exhibit good Li^+ insertion/extraction behavior tend to degrade more slowly and retain capacity more effectively (Siriroj et al., 2024).

Additionally, the electrochemical performance was evaluated by determining the specific capacity from the cyclic voltammograms (CCV) of the glass electrode, calculated using the following equation (Khajonrit et al., 2018).

$$C_{CV} = \frac{1}{vm\Delta V} \int IdV \qquad \text{Equation 4.4}$$

where V is the scan rate (mV/s), m is the active material mass (g), ΔV is the potential window (V), and I is the current response (A). The specific capacity of the glass samples, calculated from the area under the CV curve at a scan rate of 0.5 mV/s, is presented in Figure 30e, while the energy density can be calculated and the results are shown in Figure 30f. However, the specific capacity is only reported for cycles 1 through 3.

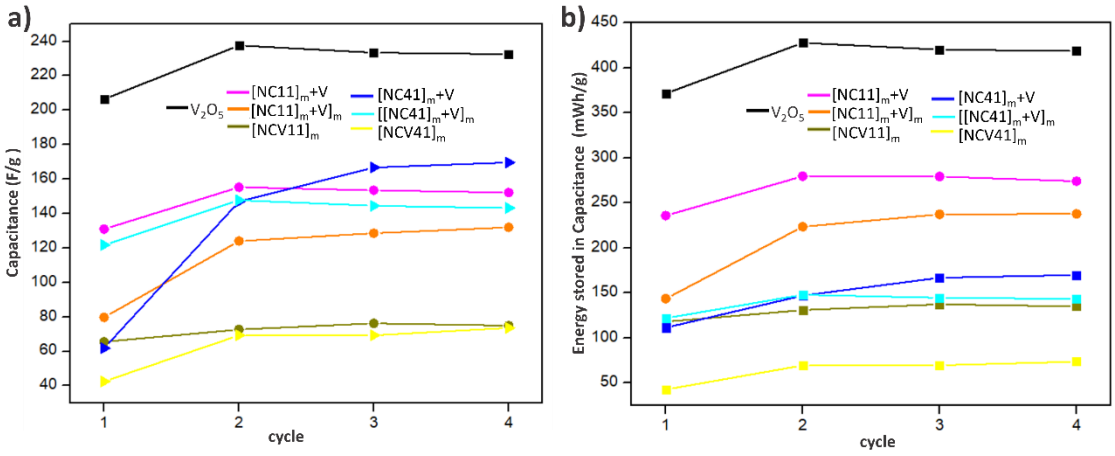

Figure 4.20 a) The capacitance and b) energy density values were measured, with a consistent scan rate of 0.5 mV/s throughout the experiment.

4.7 X-ray Absorption Near Edge Structure (XANES)

X-ray Absorption Near Edge Structure (XANES) is a powerful technique used to probe the electronic structure and local environment of atoms in a material. It focuses on the near-edge region of an X-ray absorption spectrum, typically within 50 eV of the absorption edge, providing detailed information about oxidation states, coordination geometry, and electronic transitions. XANES is particularly useful in studying the

chemical state of elements within complex systems, such as battery electrodes, catalysts, and other functional materials. By analyzing the fine structure near the absorption edge, researchers can gain insights into the local bonding environment and electronic configuration of specific atoms, helping to understand the material's properties and behavior under different conditions.

4.7.1 Verification of Oxidation States in Nickel-Mixed Glass Samples Using X-ray Absorption Near Edge Structure (XANES) Analysis

The glass sample was analyzed using X-ray Absorption Spectroscopy (XAS). The sample, prepared from a new glass film that had not yet been assembled into a coils cell, was utilized to measure the X-ray Absorption Near Edge Structure (XANES) spectrum. All glass samples were assessed for X-ray absorption in the XANES region of Ni at the K-edge, with photon energy at 409.9 ± 0.2 eV, employing transmission mode. The data obtained were processed using Athena software, yielding two forms of XANES spectra: the Normalized Spectrum and the First Derivative Spectrum, as illustrated in Figure 4.21.

From these spectra, the slope of the Normalized Spectrum and the peak position of the First Derivative Spectrum were analyzed to determine the absorption edge energy of Ni-glass in comparison to standard materials, as detailed in Table 4.3. This table reveals that nickel in the glass samples is predominantly present in the forms of Ni^{2+} and Ni^{3+}.

Furthermore, the concentrations of these oxidation states provide valuable insights into the electronic environment of nickel within the glass matrix, which can influence the material’s properties, such as conductivity and thermal stability. The average oxidation state of nickel ions in the glass samples was calculated using equations 4.5-4.7. These calculations are crucial for understanding the role of nickel in the overall glass structure and its potential applications in advanced materials and devices (Daengsakul et al., 2015).

$$\langle \%\ \text{of}\ N^{3+} \rangle = \left[\frac{\Delta E\ \text{of sample}}{\Delta E\ \text{of}\ Ni^{3+}\ \text{and}\ Ni^{2+}} \right] \times 100 \qquad \text{Equation 4.5}$$

$$\langle \%\ \text{of}\ N^{2+} \rangle = \left[1 - \frac{\Delta E\ \text{of sample}}{\Delta E\ \text{of}\ Ni^{3+}\ \text{and}\ Ni^{2+}} \right] \times 100 \qquad \text{Equation 4.6}$$

$$\langle \text{Ni oxidation state} \rangle = 3 \left[\frac{\Delta E\ \text{of sample}}{\Delta E\ \text{of}\ Ni^{3+}\ \text{and}\ Ni^{2+}} \right] + 2 \left[1 - \frac{\Delta E\ \text{of sample}}{\Delta E\ \text{of}\ Ni^{3+}\ \text{and}\ Ni^{2+}} \right] \qquad \text{Equation 4.7}$$

Table 4.3 Position of X-ray absorption of Ni-glass with standard material.

Sample of standard	Peak Position (eV)	Sample	Peak Position (eV)	Sample	Peak Position (eV)
NiO: 2+ (Calculate)	8343.20	**$[NC11]_m$**	8344.88	**$[NC41]_m$**	8343.36
$Ni(OH)_2$: 2+ (Standard)	8344.55	**$[NC11]_m$+V**	8344.67	**$[NC41]_m$+V**	8344.95
Li_2NiBO_4: 3+ (Standard)	8348.52	**$[NC11]_m$+V$]_m$**	8344.98	**$[NC41]_m$+V$]_m$**	8345.38
		[NC11+V$]_m$	8346.03	**[NC41+V$]_m$**	8345.13

Table 4.3 displays the average oxidation state calculations for the glass samples. It was found that the oxidation state of nickel in the glass is predominantly Ni^{2+} rather than Ni^{3+}, indicating a higher concentration of Ni^{2+} ions in the samples. This suggests that the nickel in the glass remains in a lower oxidation state compared to Ni^{3+}. The prevalence of Ni^{2+} over Ni^{3+} is likely due to the glass matrix composition and its stabilizing effect on Ni^{2+} ions, which favors this lower oxidation state.

The presence of a greater amount of Ni^{2+} ions can significantly influence the chemical and physical properties of the glass, such as its color, electronic conductivity, and thermal stability. For instance, Ni^{2+} ions often contribute to a more intense color

in glass materials, while also potentially enhancing its durability and resistance to thermal stress. The predominance of Ni^{2+} can also affect the glass structure at the atomic level, leading to variations in network connectivity and, consequently, the material's mechanical properties.

However, the differences in oxidation states are not substantial, as indicated by the ΔE, which represents the energy difference at the absorption edge. This relatively small ΔE between Ni^{2+} and Ni^{3+} (5.32 eV) suggests that only minor changes occur in the electronic structure, without significantly altering the glass's overall stability. Consequently, the Ni^{2+}-rich composition likely stabilizes the glass matrix, providing a beneficial balance between enhanced physical properties and controlled electronic behavior.

Table 4.4 Average oxidation numbers of nickel ions in glass samples.

Sample	*ΔE of sample (eV)	%(Ni^{2+})	%(Ni^{3+})	Average oxidation number
$[NC11]_m$	1.68	68.42	31.58	2.32
$[NC11]_m$+V	1.47	72.37	27.63	2.28
$[NC11]_m$+V$]_m$	1.78	66.54	33.46	2.33
$[NC11+V]_m$	2.60	51.13	48.87	2.49
$[NC41]_m$	0.16	96.99	3.01	2.03
$[NC41]_m$+V	1.75	67.11	32.89	2.33
$[NC41]_m$+V$]_m$	2.18	59.02	40.98	2.41
$[NC41+V]_m$	1.93	63.72	36.28	2.36

*The ΔE for Ni^{2+} and Ni^{3+} is 5.32 eV.

*ΔE represents the energy difference at the absorption edge.

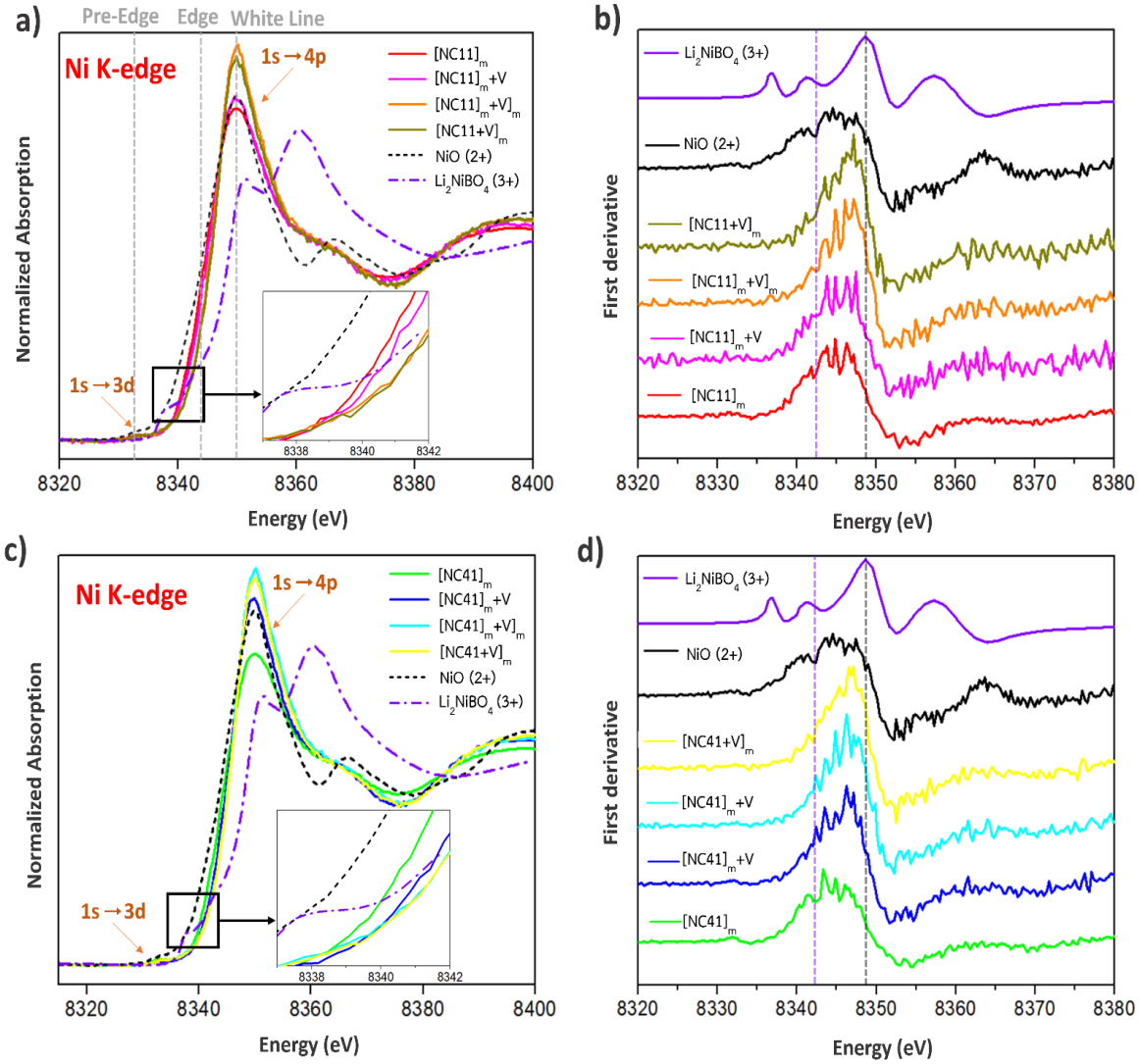

Figure 4.21 XANES spectrum a,c) Normalized Spectrum b,d) First Derivative Spectrum.

4.7.2 Verification of Oxidation States in Cobalt-Mixed Glass Samples Using X-ray Absorption Near Edge Structure (XANES) Analysis

Each glass sample was analyzed for X-ray absorption in the XANES range of Co at the K-edge, using photons with energy of 7709.0 ± 0.2 eV in transmission mode. The obtained data were analyzed with the Athena software, resulting in two distinct XANES spectra, as shown in Figure 4.22. The absorption edge position in the glass samples

closely matches the absorption position of the reference standards, as presented in Table 4.5.

Table 4.5 Position of X-ray absorption of Co-glass with standard material.

Sample of standard	Absorption position (eV)	Sample	Absorption position (eV)	Sample	Absorption position (eV)
CoO: 2+	7717.49	**$[NC11]_m$**	7717.69	**$[NC41]_m$**	7718.04
Co_3O_4: 2+,3+	7721.63	**$[NC11]_m$+V**	7718.19	**$[NC41]_m$+V**	7718.31
		$[NC11]_m$+V$]_m$	7718.00	**$[NC41]_m$+V$]_m$**	7718.30
		[NC11+V$]_m$	7718.81	**[NC41+V$]_m$**	7718.74

In order to calculate the average oxidation state of Co atoms, it is can be determined by comparing with the known standard sample as seen in Eq 4.8.

$$\langle \text{Co oxidation state} \rangle = 2.66 \left[\frac{\Delta E \text{ of sample}}{\Delta E \text{ of } Co^{2+/3+} \text{ and } Co^{2+}} \right] + 2 \left[1 - \frac{\Delta E \text{ of sample}}{\Delta E \text{ of } Co^{2+/3+} \text{ and } Co^{2+}} \right] \quad \text{Equation 4.8}$$

After calculating the average oxidation state for the glass samples presented in Table 4.6, it was found that the glass contains cobalt primarily in the oxidation states of Co^{2+} and $Co^{2+/3+}$. The results indicate that cobalt ions in the glass samples are predominantly in the Co^{2+} state rather than $Co^{2+/3+}$ suggesting a higher proportion of Co^{2+} ions over Co^{3+} ions. This finding implies that cobalt in the glass is mainly in a lower oxidation state, which can influence the chemical and physical properties of the glass, such as its structure, energy transfer capabilities, and material stability. The higher presence of Co^{2+} over Co^{3+} also reflects a chemical environment that favors nickel remaining in a lower oxidation state.

Table 4.6 Average oxidation numbers of cobalt ions in glass samples.

Sample	*ΔE of sample (eV)	%(Co^{2+})	%($Co^{2+/3+}$)	Average oxidation number
$[NC11]_m$	0.20	95.17	5.14	2.03
$[NC11]_m$+V	0.70	83.09	17.99	2.11
$[NC11]_m$+V$]_m$	0.51	87.68	13.11	2.08
[NC11+V$]_m$	1.32	68.12	33.92	2.21
$[NC41]_m$	0.55	86.71	14.14	2.09
$[NC41]_m$+V	0.82	80.19	21.07	2.13
$[NC41]_m$+V$]_m$	0.81	80.43	20.82	2.13
[NC41+V$]_m$	1.25	69.81	32.13	2.20

*ΔE of Co^{2+} and $Co^{2+/3+}$ = 4.14 eV

In Figure 4.22a, the Ni/Co-doped LBO glass and the reference NiO absorption spectrum at the Ni K-edge XANES are displayed. All Ni/Co-doped LBO glass samples show an absorption edge shift to higher energy compared to standard NiO, as noted by the main edge jump highlighted in the inset. Since the oxidation state of Ni in NiO is 2+, this shift suggests that the Ni in the glass samples has an oxidation state higher than 2+, as confirmed by the peak of the first derivative of the data (Figure 4.22b). For Co oxidation state analysis, Co_3O_4 and CoO standards were utilized to examine the Co K-edge XANES spectra in Figures 4.22 c and d. The research findings indicate that the glass spectra align with those of CoO (Co^{2+} oxidation) and Co_3O_4 (Co^{3+}), suggesting a mixed oxidation state of Co^{2+} and Co^{3+} in the Ni/Co-doped LBO glass. Additionally, linear combination fitting analysis using Athena software shows that approximately 55% of Co in the glass exists in the Co^{2+} phase, varying slightly depending on specific conditions.

This variation in Co^{2+} concentration could impact the electronic structure and potentially enhance the glass's catalytic properties. The mixed oxidation states of Ni and Co likely contribute to increased stability and conductivity in the glass matrix. This

detailed oxidation state analysis highlights the potential of Ni/Co-doped LBO glasses for applications that benefit from tailored electronic and structural characteristics.

The XANES analysis revealed that cobalt in Ni/Co-doped LBO glasses predominantly exists in the Co^{2+} state, with mixed oxidation states contributing to the material's stability and conductivity. Nickel was found to have a higher oxidation state than NiO, further influencing the electronic structure of the glass. These findings highlight the potential of Ni/Co-doped LBO glasses for applications requiring enhanced catalytic and electronic properties.

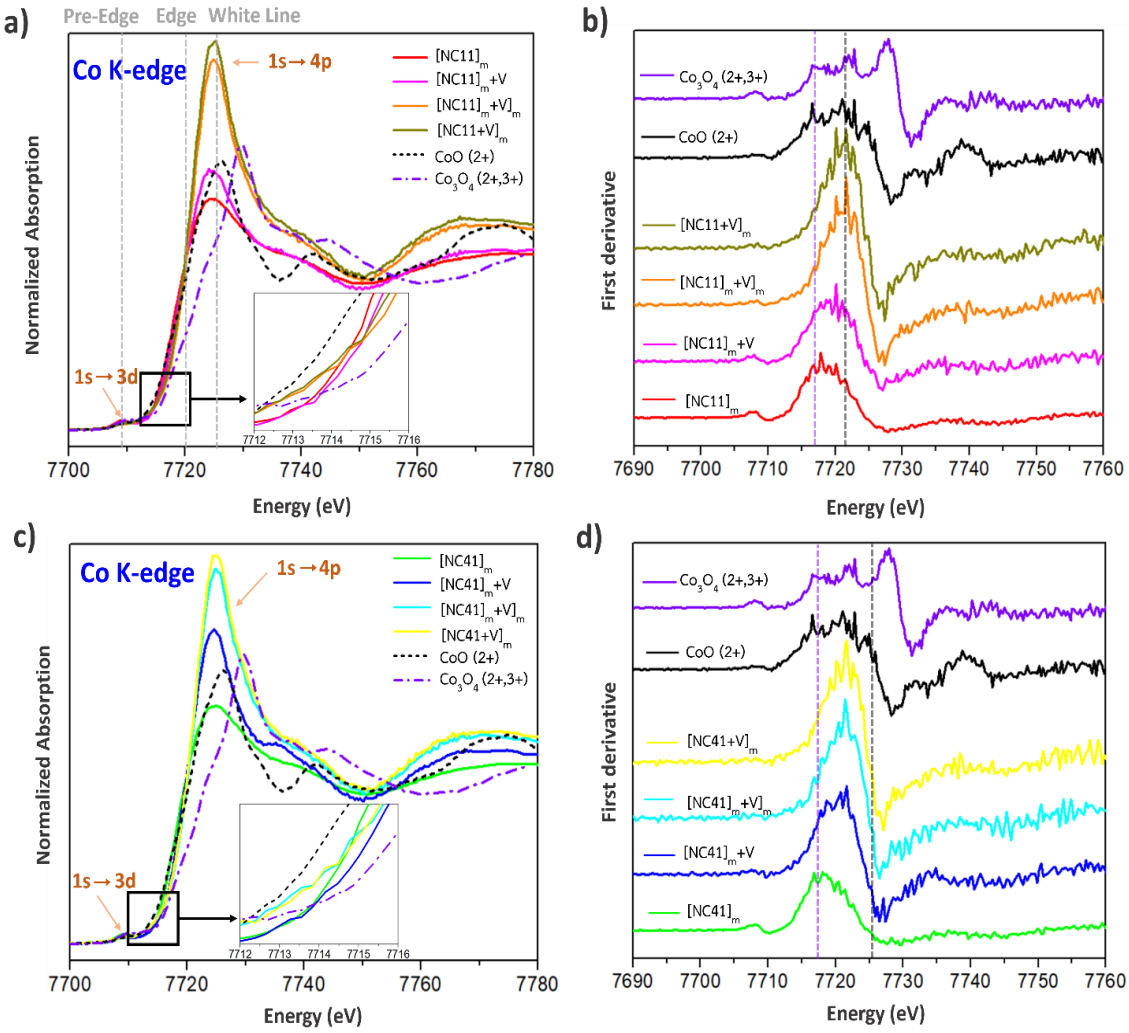

Figure 4.22 XANES spectrum a,c) Normalized Spectrum b,d) First Derivative Spectrum.

4.7.3 Verification of Oxidation States in Vanadium-Mixed Glass Samples Using X-ray Absorption Near Edge Structure (XANES) Analysis

All glass samples were analyzed for X-ray absorption in the V K-edge XANES range using photons with an energy of 5465.0 ± 0.2 eV, measured in transmission mode. The resulting data was processed using the Athena software, yielding two distinct XANES spectra, as shown in Table 4.7. The absorption edge positions of the glass samples, compared to standard compounds, are listed in Table 8, with edge positions lying between those of VO_2 and V_2O_5. This indicates that the glass samples contain vanadium in mixed oxidation states of V^{4+} and V^{5+}.

To calculate the average oxidation state of vanadium atoms, a comparison with known standard samples can be used, as demonstrated in Equation 4.9.

$$\langle \text{V oxidation state} \rangle = 5\left[\frac{\Delta E \text{ of sample}}{\Delta E \text{ of } V^{5+} \text{ and } V^{4+}}\right] + 4\left[1 - \frac{\Delta E \text{ of sample}}{\Delta E \text{ of } V^{5+} \text{ and } V^{4+}}\right] \quad \text{Equation 4.9}$$

Table 4.7 Position of X-ray absorption of V-glass with standard material.

Sample of standard	Absorption position (eV)	Sample	Absorption position (eV)	Sample	Absorption position (eV)
V_2O_3: 3+	5479.88	$[NC11]_m$+V	5481.54	$[NC41]_m$+V	5481.51
VO_2: 4+	5480.63	$[NC11]_m$+V$]_m$	5481.37	$[NC41]_m$+V$]_m$	5481.22
V_2O_5: 5+	5481.77	[NC11+V$]_m$	5481.24	[NC41+V$]_m$	5481.21

The glass samples were found to contain a higher amount of V^{5+} compared to V^{4+}, with the average oxidation state of vanadium shown in Table 4.8. The presence of V^{5+} in the glass samples aligns with the findings of (Nibel, Schmidt, and Gubler, 2014), indicating that vanadium in these samples primarily exists in a high oxidation state (V^{5+}).

This suggests that vanadium in the glass has undergone significant electron loss. The higher proportion of V^{5+} relative to V^{4+} can influence the chemical properties of the glass. The dominance of V^{5+} in the glass matrix may contribute to enhanced catalytic properties and greater stability under oxidative conditions. Additionally, the higher oxidation state could affect the glass's electronic structure, potentially improving its conductivity and suitability for advanced applications.

Table 4.8 Average oxidation numbers of vanadium ions in glass samples.

Sample	*ΔE of sample (eV)	%(V^{4+})	%(V^{5+})	Average oxidation number
$[NC11]_m$+V	0.91	20.18	79.82	4.80
$[NC11]_m$+V$]_m$	0.74	35.09	64.91	4.65
[NC11+V$]_m$	0.61	46.49	53.51	4.54
$[NC41]_m$+V	0.88	22.81	77.19	4.77
$[NC41]_m$+V$]_m$	0.59	48.25	51.75	4.52
[NC41+V$]_m$	0.58	49.12	50.88	4.51

*ΔE of $V^{4+}$and V^{5+} = 1.14 eV

According to the XANES data, nearly all vanadium compounds exist predominantly as V5+ upon synthesis and are reduced to V^{4+} during testing. The oxidation state may change as indicated by the XRD data, which suggests structural modifications that occur when lithium ions are transported from the cathode to the anode during the charging process. As a result of this ion transport, vanadium undergoes further oxidation, transitioning from V^{4+} to V^{5+}.

During discharging, there is a noticeable low-energy shift in the absorption curves, which revert to their original position upon recharging. The pre-edge feature corresponds to the dipole-forbidden 1s to 3d transition, whereas the post-edge peak is associated with the dipole-allowed 1s to 4p transition. Changes in the dipole-forbidden transition typically have low intensity or may not be visible in the spectrum,

while the dipole-allowed transition generally exhibits high intensity and is easily observable. The intensity of the pre-edge feature is sensitive to the valence state of the central vanadium atoms, the coordination environment, and the symmetry of the polyhedron. The energy position of the post-edge peak, or white line, reflects the valence state of the central vanadium atoms.

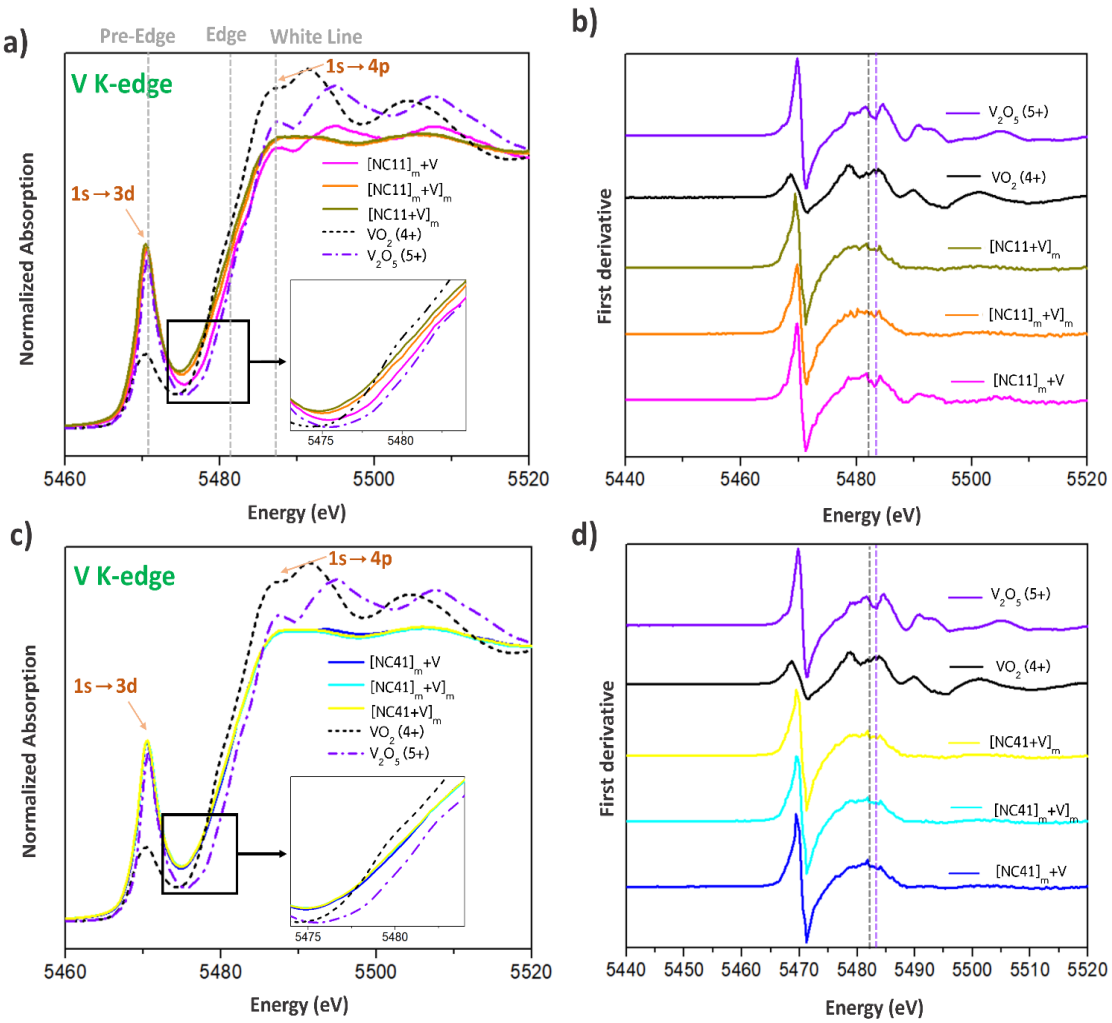

Figure 4.23 XANES spectrum a,c) Normalized Spectrum b,d) First Derivative Spectrum.

In the discharge process of lithium-ion batteries, XANES spectra reveal a decrease in the intensity of the pre-edge peak and an increase in the post-edge peak intensity. The reduction in the pre-edge peak intensity is attributed to an increase in the occupancy of vanadium d orbitals due to lithium insertion, which enhances the

symmetry of the vanadium ions in the VO_5 structure during discharge. The energy position of the post-edge peak also signifies a decrease in the oxidation state of vanadium ions, indicating that the vanadium ions receive electrons from lithium insertion, thereby reducing their oxidation state.

4.8 X-ray Absorption Fine Structure (EXAFS)

X-ray Absorption Fine Structure (EXAFS) is a powerful spectroscopic technique used to investigate the local structure around specific absorbing atoms in a material. This method involves measuring the absorption of X-rays as a function of energy, allowing researchers to obtain detailed information about the coordination environment, bond lengths, and the type of neighboring atoms surrounding the absorbing species. EXAFS provides insights into the structural and electronic properties of various materials, making it invaluable in fields such as materials science, chemistry, and solid-state physics. By analyzing the oscillatory features in the absorption spectrum, scientists can derive quantitative information regarding atomic distances and the disorder within a sample, facilitating a deeper understanding of the material's behavior and interactions at the atomic level.

4.8.1 X-ray Absorption Fine Structure (EXAFS) Analysis of Nickel-Mixed Glass Samples

The sample was analyzed by measuring the X-ray absorption spectrum in the Extended X-ray Absorption Fine Structure (EXAFS) region at the Ni K absorption edge using photons with an energy of 409.9 ± 0.2 eV in transmission mode. The data obtained were initially processed with the Athena software and subsequently analyzed further with Artemis. Additionally, crystal data for Lithium Cobalt Nickel Oxide (Li_2CoNiO_4), expected to form within the glass sample, were downloaded from the Materials Project website using the model Li_2CoNiO_4-mp-753536. The corresponding structure is shown in Figure 4.24.

Li_2CoNiO_4 crystallizes in the orthorhombic Imma space group, with a structure derived from beta polonium. The material features two inequivalent Li^{1+} sites, both forming LiO_6 octahedra that share corners and edges with CoO_6 and NiO_6 octahedra. The octahedral tilt angles range between 5-9°, and bond lengths for Li-O, Co-O, and Ni-O vary slightly, reflecting slight distortions in the structure. Co^{4+} and Ni^{2+} are both coordinated by six O^{2-} atoms, forming CoO_6 and NiO_6 octahedra. There are two distinct O^{2-} sites, each involved in bonding to Li^{1+}, Co^{4+}, and Ni^{2+}, forming complex edge- and corner-sharing octahedra.

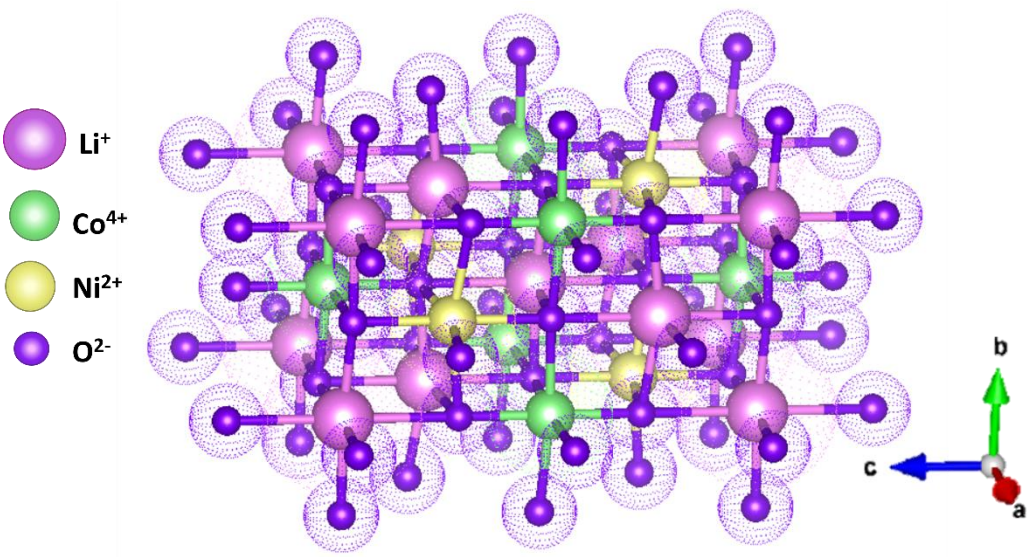

Figure 4.24 Crystal structures of Li_2CoNiO_4 Model: mp-753536.

Li_2CoNiO_4 (CAS number: 753536) is a compound that typically crystallizes in a layered oxide structure, where lithium ions (Li^+) are intercalated between layers of metal oxides formed by cobalt (Co) and nickel (Ni). The structure of this material is similar to other layered lithium transition metal oxides, such as $LiCoO_2$ or $LiNiO_2$, which are commonly used in battery applications due to their ability to reversibly insert and remove lithium ions.

In the Li_2CoNiO_4 model, cobalt and nickel ions occupy octahedral sites in a mixed transition metal oxide framework. This creates a strong bonding network with oxygen atoms (O^{2-}) that form a closely packed lattice. The lithium ions, which are

relatively mobile, can move between these layers, making this material potentially useful for electrochemical applications such as lithium-ion batteries.

Using the crystal structure data, the program identifies the scattering paths of atoms surrounding nickel, the absorber, and fits these paths to the experimental data from the glass sample. In this fitting process, only single scattering paths with high amplitude are selected, as lower amplitude paths have minimal impact on the R-factor, a statistical measure of the difference between the model and experimental data. Once the fitting is complete, the Fourier-transformed EXAFS spectrum of the NiO-doped glass sample is obtained, as illustrated in Figure 4.25.

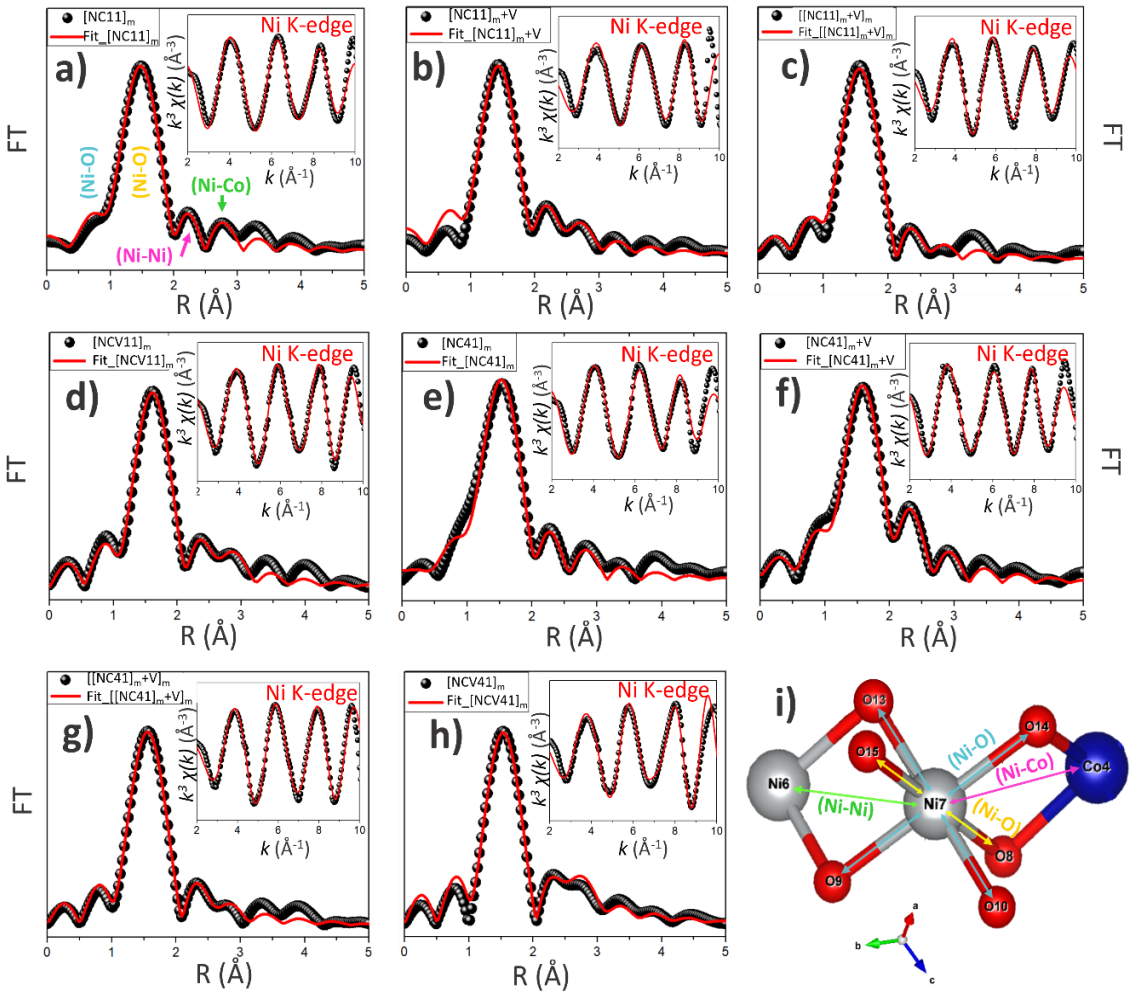

Figure 4.25 a-h) EXAFS spectra and fitting at Ni K-edge of sample. i) The model used to observe the atomic distances.

Table 4.9 Presents the optimal fitting parameters for the NiO-doped glass sample compared with data from Li_2CoNiO_4.

Sample	Paths	N	S_0^2	σ^2	R (A^o)	ΔE_0 (eV)	R-factor
$[NC11]_m$	Ni-O	6	0.737	0.00504	2.04159	-2.923	0.0118621
	Ni-Ni	2	0.737	0.02809	2.45422		
	Ni-Co	4	0.737	0.06502	2.69255		
$[NC11]_m$+V	Ni-O	6	1.000	0.00758	2.06955	-2.218	0.0040836
	Ni-Ni	2	1.000	0.00743	2.53744		
	Ni-Co	4	1.000	0.02114	2.78758		
$[NC11]_m$+V$]_m$	Ni-O	6	1.000	0.00416	2.07267	-0.767	0.0054326
	Ni-Ni	2	1.000	0.00742	2.48465		
	Ni-Co	4	1.000	0.01404	2.69021		
$[NC11+V]_m$	Ni-O	6	1.000	0.00510	2.05305	-4.330	0.0046821
	Ni-Ni	2	1.000	0.01035	2.53507		
	Ni-Co	4	1.000	0.02042	2.79672		
$[NC41]_m$	Ni-O	6	0.950	0.01018	2.05467	-2.479	0.0139459
	Ni-Ni	2	0.950	0.01587	2.40212		
	Ni-Co	4	0.950	0.02233	2.60948		
$[NC41]_m$+V	Ni-O	6	1.000	0.00587	2.04330	-4.196	0.0018229
	Ni-Ni	2	1.000	0.01162	2.46637		
	Ni-Co	4	1.000	0.02747	2.78699		
$[NC41]_m$+V$]_m$	Ni-O	6	1.000	0.00681	2.05599	-2.112	0.0038975
	Ni-Ni	2	1.000	0.01025	2.50072		
	Ni-Co	4	1.000	0.02190	2.80499		
$[NC41+V]_m$	Ni-O	6	1.000	0.00512	2.00044	-9.677	0.0077284
	Ni-Ni	2	1.000	0.00536	2.53530		
	Ni-Co	4	1.000	0.01053	2.78658		

**Note: Acceptable parameter ranges are as follows: S_0^2 (0.7–1.2), ΔE_0 (-10 to 10 eV), R-factor (<0.05), and σ^2 (>0.003).

This analysis allows for a more accurate understanding of the local atomic environment around nickel within the glass structure. The high-amplitude scattering paths contribute significantly to understanding the bonding and coordination characteristics of Ni in the doped glass sample.

After fitting the paths, the best-fit parameters obtained were R (the distance between surrounding atoms and the absorber), $\boldsymbol{\sigma}^2$ (the Debye-Waller factor), $\boldsymbol{S_0^2}$ (the scattering amplitude), ΔE_0 (the energy shift at the absorption edge), and the R-factor (a statistical measure indicating the difference between the model and experimental data) for all eight glass samples, as shown in Table 4.9. The parameters derived from the fitting are within acceptable ranges for each sample, and the spectrum lines of each glass sample closely match their best-fit lines. This indicates that the nickel ions in the glass samples have a structural environment similar to that of Ni-O bonding, with bond lengths for Ni-O (1.96 Å), Ni-Ni (2.87 Å), and Ni-Co (2.89 Å) closely aligning with those in the Li_2CoNiO_4 structure.

4.8.2 X-ray Absorption Fine Structure (EXAFS) Analysis of Cobalt-Mixed Glass Samples

Based on the crystal structure data of Li_2CoNiO_4, the program generates possible paths and then fits them to the experimental data obtained from the glass sample. Upon fitting the glass sample against the Li_2CoNiO_4 model paths, the Fourier-transformed EXAFS spectrum of the glass doped with Co_3O_4 is obtained, compared with the best-fit line, as shown in Figure 4.26, and the fitting parameters presented in Table 4.10. It was found that the parameters $\boldsymbol{\sigma}^2$, $\boldsymbol{S_0^2}$, and ΔE_0 for all samples lie outside the acceptable range. Additionally, an analysis of bond lengths in the sample shows Co–O (1.94 Å), Co–Co (2.86 Å), and Co–Ni (2.89 Å) bonds, which are relatively long within the Li_2CoNiO_4 structure. This suggests that cobalt ions in the glass sample are in a structural arrangement similar to that of the Li_2CoNiO_4 structure.

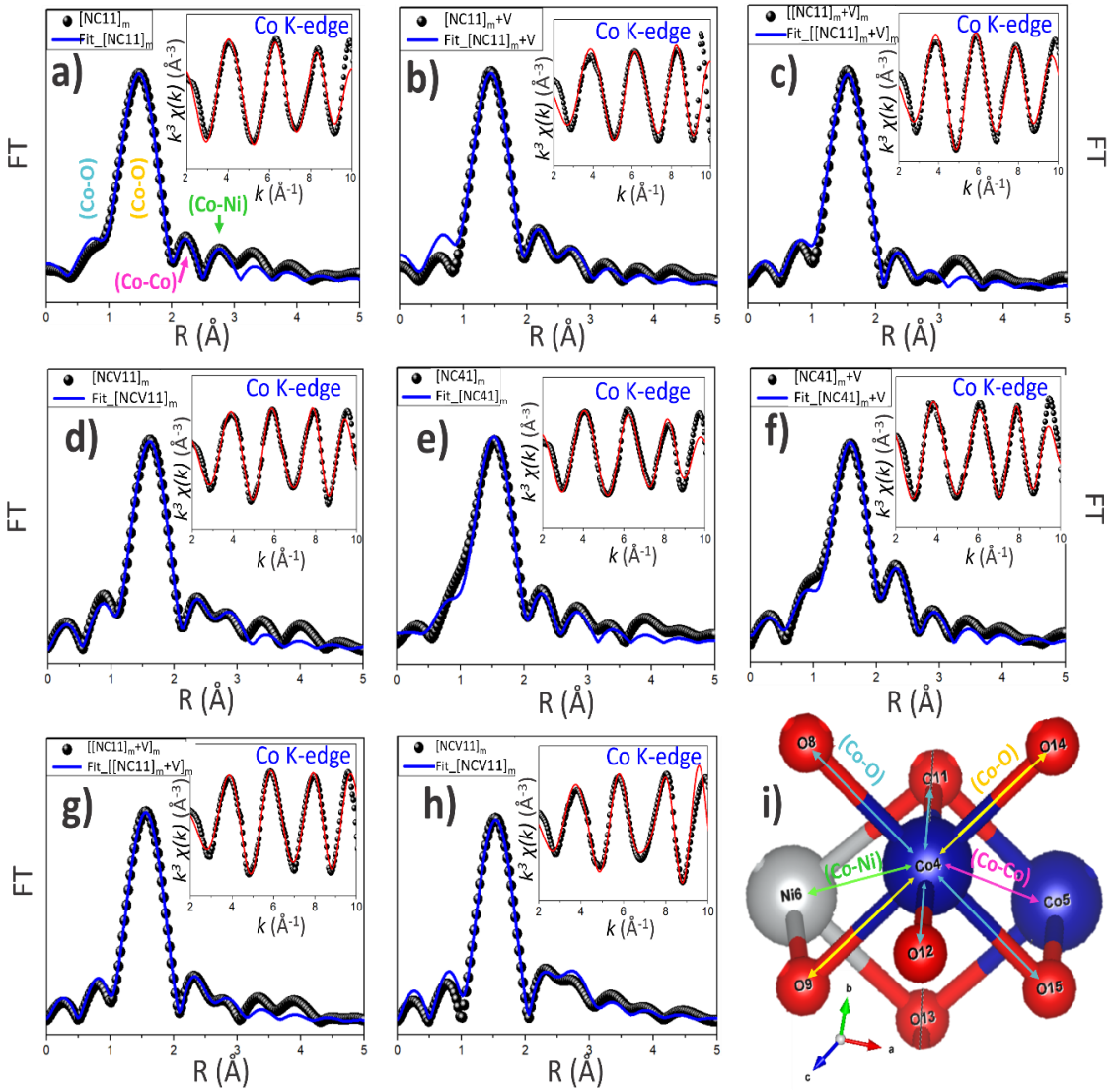

Figure 4.26 a-h) EXAFS spectra and fitting at Co K-edge of sample. i) The model used to observe the atomic distances.

The analysis suggests that Co ions in the glass matrix adopt a coordination environment similar to that of Li_2CoNiO_4, enhancing the glass's structural stability. Observed bond lengths, especially the Co–O, Co–Co, and Co–Ni distances, suggest slight distortion compared to the ideal crystal structure, likely due to the glass's amorphous nature. This bond length variation can influence the glass's electronic and magnetic properties.

Table 4.10 Presents the optimal fitting parameters for the Co_3O_4-doped glass sample compared with data from Li_2CoNiO_4.

Sample	Paths	N	S_0^2	σ^2	R (A^o)	ΔE_0 (eV)	R-factor
[NC11]$_m$	Co-O	6	0.710	0.00926	1.99420	-2.605	0.008685
	Co-Co	2	0.710	0.01320	2.37512		
	Co-Ni	4	0.710	0.02278	2.60142		
[NC11]$_m$+V	Co-O	6	0.750	0.00690	1.98222	-9.263	0.0067937
	Co-Co	2	0.750	0.01088	2.36073		
	Co-Ni	4	0.750	0.02007	2.61954		
[NC11]$_m$+V]$_m$	Co-O	6	0.780	0.00502	2.05960	-3.936	0.0074191
	Co-Co	2	0.780	0.03347	2.65349		
	Co-Ni	4	0.780	0.03231	2.81446		
[NC11+V]$_m$	Co-O	6	0.842	0.00562	2.08843	0.356	0.0025018
	Co-Co	2	0.842	0.00939	2.53352		
	Co-Ni	4	0.842	0.01454	2.78645		
[NC41]$_m$	Co-O	6	0.700	0.01038	2.01583	-0.885	0.0037887
	Co-Co	2	0.700	0.01189	2.43531		
	Co-Ni	4	0.700	0.02227	2.67789		
[NC41]$_m$+V	Co-O	6	1.000	0.01223	2.08652	-0.208	0.0014706
	Co-Co	2	1.000	0.01066	2.49280		
	Co-Ni	4	1.000	0.02691	2.73803		
[NC41]$_m$+V]$_m$	Co-O	6	0.703	0.00141	2.05227	-2.921	0.0025829
	Co-Co	2	0.703	0.03397	2.45121		
	Co-Ni	4	0.703	0.02340	2.77207		
[NC41+V]$_m$	Co-O	6	0.830	0.00352	2.07041	-4.387	0.0104582
	Co-Co	2	0.830	0.00869	2.45899		
	Co-Ni	4	0.830	0.01141	2.71864		

**Note: Acceptable parameter ranges are as follows: S_0^2 (0.7–1.2), ΔE_0 (-10 to 10 eV), R-factor (<0.05), and σ^2 (>0.003).

Deviations in fitting parameters (σ^2, S_0^2, and ΔE_0) from the acceptable range reflect differences between the model and the glass's local Co environment. These discrepancies likely stem from the glass's inherent structural disorder, affecting Co coordination and bonding. Overall, the glass's similarity to Li_2CoNiO_4, combined with its unique structural properties, highlights its potential for further investigation in advanced materials research.

4.8.3 X-ray Absorption Fine Structure (EXAFS) Analysis of Vanadium-Mixed Glass Samples

The sample plate was measured for its X-ray absorption spectrum in the Extended X-ray Absorption Fine Structure (EXAFS) region at the K-absorption edge of vanadium, using photons with an energy of 5465.0 ± 0.2 eV in transmission mode. The collected data was then analyzed using the Athena software, followed by further analysis with Artemis. Additionally, the crystal data for V_2O_5 was downloaded using Model: mp-25279, which is expected to form in this glass sample group. The V_2O_5 structure is displayed in Figure 4.27.

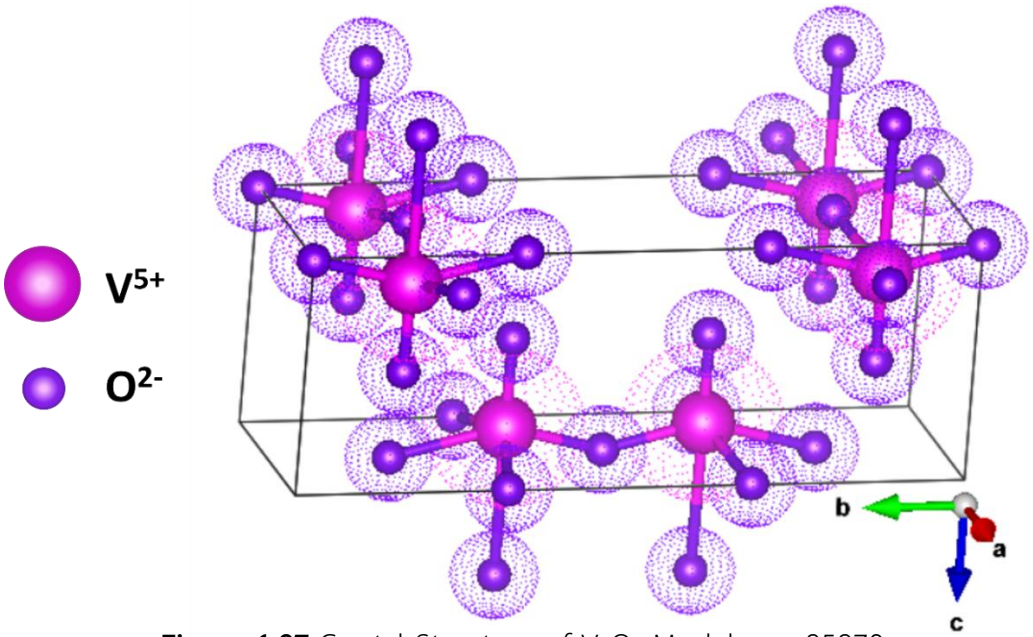

Figure 4.27 Crystal Structure of V_2O_5 Model: mp-25279.

V_2O_5 (vanadium pentoxide) with material ID mp-25279 crystallizes in an orthorhombic structure and belongs to the Pmmn space group. The structure consists

of layered sheets of vanadium (V) and oxygen (O), where vanadium atoms are coordinated in distorted octahedra formed by six oxygen atoms. These VO_6 octahedra are edge- and corner-sharing, creating a layered structure with strong in-plane V-O bonds and weaker van der Waals interactions between layers.

Table 4.11 The optimal fitting parameters for the glass sample doped with V_2O_5 were determined by comparison with reference data from V_2O_5.

Sample	Paths	N	S_0^2	σ^2	R (A°)	ΔE_0 (eV)	R-factor
$[NC11]_m$+V	V-O	1	0.700	0.00004	1.87410	-3.159	0.0241498
	V-O	4	0.700	0.02320	1.68093		
	V-O	1	0.700	0.22544	2.55790		
	V-V	1	0.700	0.01089	2.97310		
$[NC11]_m$+V]$_m$	V-O	1	0.700	0.00268	1.57724	8.313	0.0485365
	V-O	4	0.700	0.01307	1.86090		
	V-O	1	0.700	0.30218	2.65581		
	V-V	1	0.700	0.00001	3.06033		
[NC11+V]$_m$	V-O	1	1.000	0.00273	1.53027	-5.027	0.0325568
	V-O	4	1.000	0.01954	1.78401		
	V-O	1	1.000	0.00006	2.66472		
	V-V	1	1.000	0.00976	2.98644		
$[NC41]_m$+V	V-O	1	1.000	0.00056	1.52996	-6.131	0.0785836
	V-O	4	1.000	0.01852	1.77016		
	V-O	1	1.000	0.00263	2.66446		
	V-V	1	1.000	0.01369	2.99292		
$[NC41]_m$+V]$_m$	V-O	1	0.700	-0.00136	1.57430	0.417	0.0216169
	V-O	4	0.700	0.01113	1.85134		
	V-O	1	0.700	0.27030	2.67892		
	V-V	1	0.700	0.00821	3.06099		

**Note: Acceptable parameter ranges are as follows: S_0^2 (0.7–1.2), ΔE_0 (-10 to 10 eV), R-factor (<0.05), and σ^2 (>0.003).

Based on the crystal structure data, the program generates the scattering paths of atoms surrounding iron and fits them to the experimental data from the glass sample. After fitting the glass sample to the V_2O_5 model paths, the Fourier-transformed EXAFS spectrum of the V-doped glass is obtained and compared with the best-fit line, as shown in Figure 4.28, with the fitting parameters listed in Table 4.11. It was observed that the parameters σ^2, S_0^2, and ΔE_0 For all V-doped glass samples, the results fall outside the acceptable range; however, the spectrum of each glass sample shows limited similarity to the best-fit line. Further fitting attempts with models such as $Li_2V_6O_{15}$ and others were conducted, but no model provided a close match between the sample and the best-fit spectrum. This indicates that the vanadium ions in the glass sample are embedded in a highly complex structural arrangement. This suggests that the structural environment of vanadium in the glass matrix is significantly disordered. The lack of a suitable model fit implies that vanadium ions may exist in multiple coordination states or local environments. Further investigations using advanced structural analysis techniques are necessary to better understand the atomic arrangement of vanadium in the glass sample.

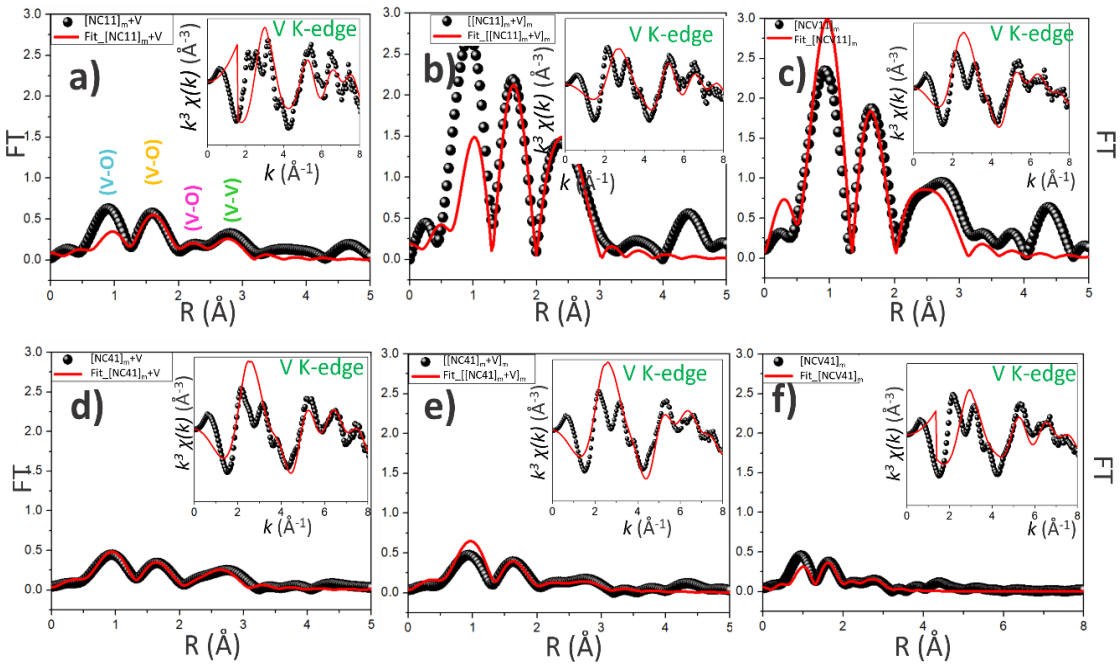

Figure 4.28 EXAFS spectra and fitting at V_2O_5 K-edge of sample.

4.9 In situ XANES analyses of V_2O_5 upon Li^+ intercalation/de-intercalation.

In situ XANES analysis of V_2O_5 during Li^+ intercalation and de-intercalation provides insights into the changes in the oxidation state and local structure of vanadium atoms in V_2O_5 while the material is actively undergoing these processes. This X-ray Absorption Near Edge Structure (XANES) spectroscopy reveals how the electronic structure and local environment around the vanadium atoms are altered during lithium insertion and removal. Understanding these changes is crucial for improving the performance and longevity of lithium-ion batteries, as it helps in optimizing the material's behavior and efficiency during battery operation.

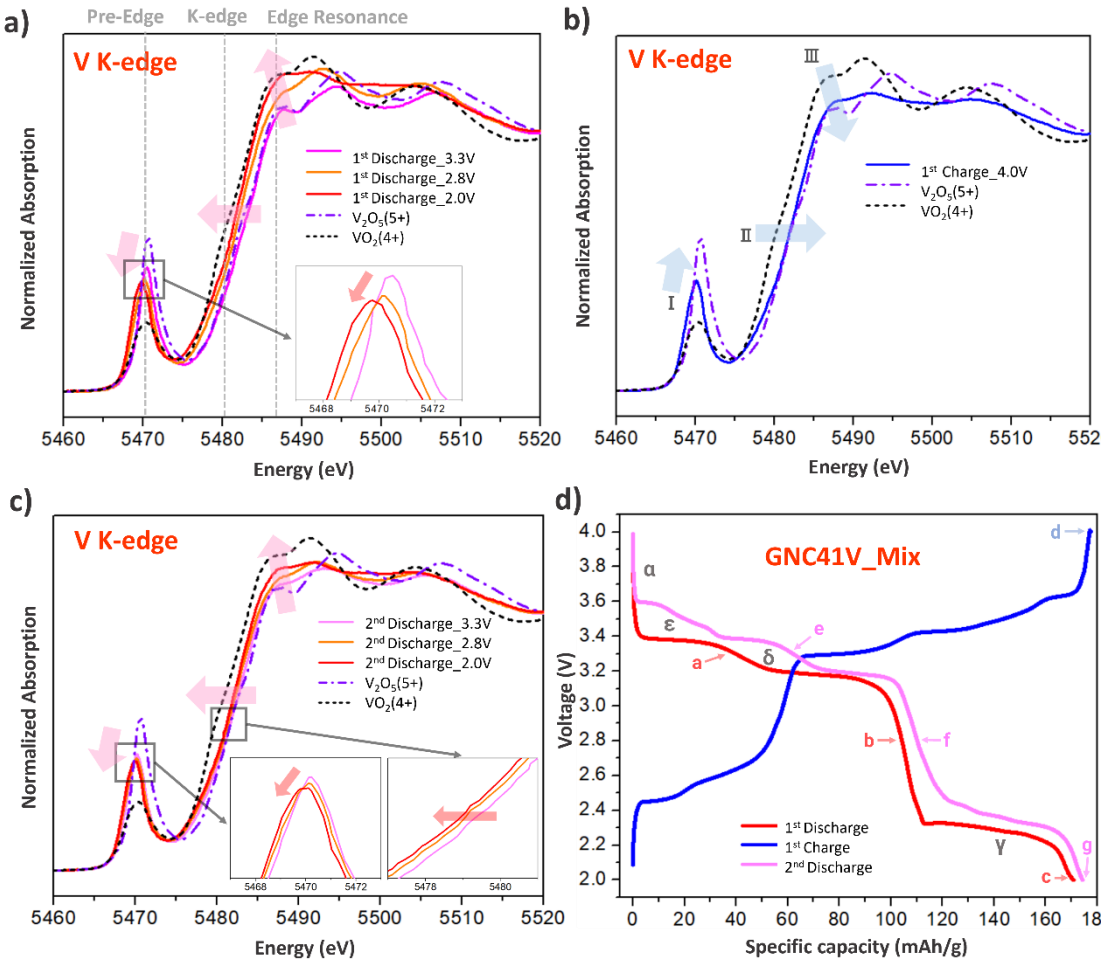

Figure 4.29 Normalized XANES Spectrum: a,c) Discharge and b) Charge; d) Voltage-Capacity Curves for Charge and Discharge Cycles.

In this study, the $[NC41]_m$+V sample was used to clearly observe the phase transitions of the V_2O_5 crystal structure. Phase changes were examined across voltage ranges of 3.3, 2.8, and 2.0 V, with a graph displaying the charge and discharge behavior of the cathode as a function of cycling shown in Figure 2.29d. For this experiment, a hole was drilled in the coin cell on the cathode side to measure X-ray Absorption Spectroscopy (XAS) in Transmission Mode (TM-XAS), with epoxy applied to prevent electrolyte leakage from the cell.

To confirm the oxidation state changes and the chemical environment around vanadium atoms within the V_2O_5 crystal, XANES analysis was conducted during the first discharge and charge cycle at 0.1 C. The Vanadium K-edge XANES spectrum can be divided into three primary components: the pre-edge, K-edge, and edge resonance (white line), labeled as Ⅰ, Ⅱ, and Ⅲ, respectively, in Figure 4.29b. The first discharge, marked as "1st Discharge," is illustrated in Figure 4.29a.

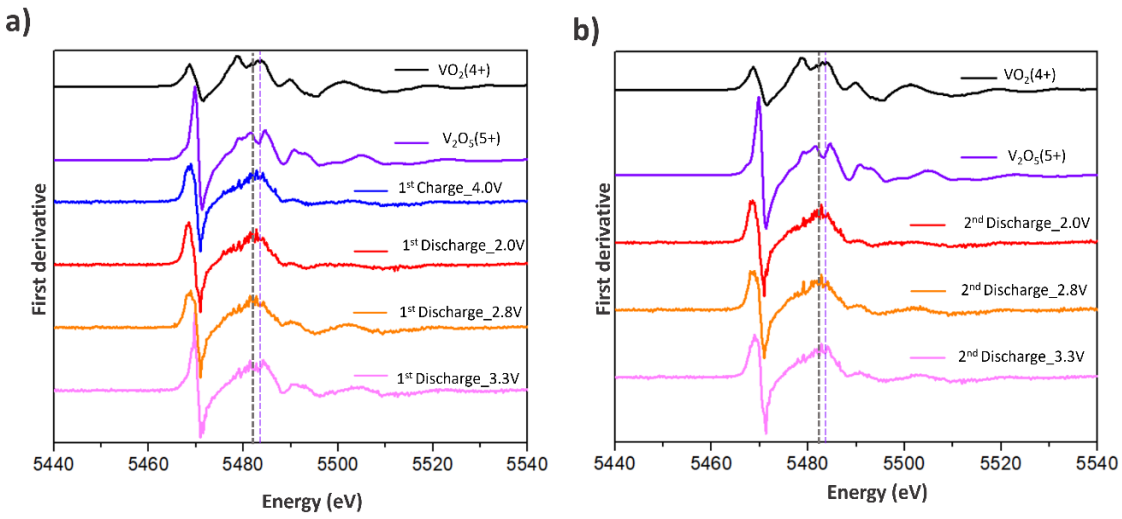

Figure 4.30 First Derivative Spectrum of the XANES Spectrum.

Changes in the pre-edge peak (Ⅰ) indicate a reduction in intensity and a shift towards lower energy levels (1s ⟶ 3d), following the red arrow on the graph. This shift signifies that Li^+ ions intercalate into the V_2O_5 structure, enhancing local symmetry around the vanadium atoms. The intensity of this pre-edge peak is sensitive to

geometric symmetry alterations, directly relating to the distortion in the VO_5 square pyramidal structure (Palanisamy, Um, Jeong, and Yoon, 2016). During the initial discharge, the K-edge (Ⅱ) progressively shifts to lower energies as more Li^+ is incorporated into the Lix V_2O_5 structure, indicating a reduction in the average oxidation state of vanadium. This corresponds with the increased amount of Li^+ intercalated into V_2O_5, where vanadium receives electrons from lithium, lowering its oxidation state.

Lastly, changes in the edge resonance (Ⅲ) reflect a decrease in intensity and a shift towards lower energy levels (1s ⟶ 4p), as shown by the red arrow in the graph. This shift is noticeable upon Li^+ insertion, resulting from the reduction in vanadium's oxidation state and indicating an increase in valence and enhanced local symmetry around the vanadium atoms in the structure.

The initial charging process, known as the 1st Charge, is shown in Figure 2.29b. The observed XANES spectrum during this charge process contrasts with the discharge process, as indicated by the blue arrows. The shift of the pre-edge peak (Ⅰ) toward higher energy (1s ⟶ 3d) with an increase in intensity indicates a shortening of the vanadyl (V=O) bond length. This shortening increases the distortion within the local structure and reduces the symmetry in the VO_5 square pyramid. Meanwhile, the shift of the K-edge (Ⅱ) to higher energy during charging signifies an increase in the oxidation state of vanadium atoms, consistent with the calculated oxidation states shown in Table 4.12. Additionally, the increase in intensity and the shift in edge resonance (Ⅲ) toward higher energy (1s ⟶ 4p) correspond with the extraction of Li+ ions and the associated increase in vanadium oxidation state, reflecting a reduction in valence and an improvement in local structural symmetry around vanadium. After the first cycle, the vanadium oxidation state returns close to its original state. In the subsequent 2nd Discharge cycle, depicted in Figure 4.29c, similar spectral changes are observed, indicating a consistent structural behavior. Following the first cycle, the distortion level of the VO_5 square pyramid decreases, and the symmetry of oxygen around vanadium increases slightly compared to the initial state. The XANES results, comparing between the pristine and fully charged states, show a partial restoration of electronic and local

structure in the composite as Li^+ ions are inserted and extracted (Palanisamy et al., 2016). This suggests that in the second charge cycle, Li ions are not completely removed from the intermediate layers, likely due to the formation of a solid-electrolyte interphase (SEI) film, leading to irreversible capacity loss (H. Wang et al., 2017).

Table 4.12 The calculated valence state of V_2O_5 ions according to the edge energy shift positions.

Steps in the Volt Range	V_2O_3: 4+ (%)	V_2O_5: 5+ (%)	V oxidation state
a) 1st Discharge at 3.3V	33.33	66.67	**4.67**
b) 1st Discharge at 2.8V	42.98	57.02	**4.57**
c) 1st Discharge at 2.0V	81.58	18.42	**4.18**
d) 1st Charge at 4.0V	73.68	26.32	**4.26**
e) 2nd Discharge at 3.3V	31.58	68.42	**4.68**
f) 2nd Discharge at 2.8V	29.82	70.18	**4.70**
g) 2nd Discharge at 2.0V	14.91	85.09	**4.85**

The energy shifts of V K-edge XANES spectra have been used to determine the valence state of the absorbing vanadium atom. According to Table 4.12, the calculated valence state from Equation X shows that the average oxidation state of V_2O_5 decreases during the initial discharge (a)–(c), as measured at 3.3, 2.8, and 2.0 V. This reduction during discharge indicates that V^{5+} ions in V_2O_5 are reduced to V^{4+}, with an overall decrease of approximately 10.49% in V^{5+} between 3.3 V and 2.0 V, consistent with previous K-edge XANES analysis. In contrast, upon charging to 4.0 V (d), the calculated valence state of 4.26, derived from XANES, suggests the presence of excess oxygen within the crystal structure, as there is a higher proportion of V^{4+} relative to V^{5+}. This means that during charging, V^{4+} ions are oxidized back to V^{5+}, then transition to V^{4+} when Li is removed (Mansour, Smith et al., 2002). During the second discharge (e)–(g),

the calculated oxidation state increases by approximately 3.63% at measurements of 3.3, 2.8, and 2.0 V, indicating that nearly all V^{4+} ions are re-oxidized to V^{5+}.

In crystalline materials, multiple coordination shells are readily identifiable, while in amorphous materials, only the first coordination shell is distinctly observed. Despite this, the overlapping first-shell distances between the two samples indicate that the amorphous material retains a tetrahedral coordination environment, albeit with significant disorder in the orientations of the Ge tetrahedra, which share corners or edges. This structural disorder plays a crucial role in determining the overall properties of the glass material (Sayers, Stern, and Lytle, 1971).